Experimental and numerical characterization of a ceramic matrix composite shroud segment under impact loading

Florence Nyssen, Nicolas Tableau, Deborah Lavazec, Alain Batailly

Experimental and numerical characterization of a ceramic matrix composite shroud segment under impact loading

Nyssen Florence[1], Tableau Nicolas[2], Lavazec Déborah[2], Batailly Alain[1]

Abstract

This work focuses on the experimental and numerical characterization of stress levels within a shroud segment made of ceramic matrix composite (CMC) material undergoing repeated blade contacts. The dedicated experimental set-up consists in a rotating disk with three notched mock blades that impact the shroud segment as they rotate. The underplatform on which the shroud is fixed progressively gets closer to the blades, so that the abradable layer deposited onto the shroud is progressively worn out from a blade revolution to another. Four sensors, located under the shroud segment, are used to record forces during the experiments. Different blade/shroud relative positions are tested, in such a way that impacts may occur at distinct locations. In addition to the experimental tests, a numerical model is built based on both reduced order models of the blade and the shroud segment, in order to numerically predict the forces at the four sensors. This numerical model is first calibrated based on a single reference test case to retrieve the same force magnitude at each sensor. Then, the other tests are simulated using the calibrated model. Predicted contact forces are in good agreement with experimental data, which validates the numerical model. Finally, simulations are carried out considering engine-like conditions, which could not be reproduced using the experimental test bench. The influence of several parameters (radial velocity, impact location, number of blades in contact and angular speed) is analyzed in detail.

Keywords

turbine shroud; ceramic matrix composites; impact loading; rotor-stator interactions

1 - Department of Mechanical Engineering, École Polytechnique de Montréal, P.O. Box 6079, Succ. Centre-Ville, Montréal, Québec, Canada H3C 3A7
2 - Safran Aircraft Engines, Villaroche, France

Caractérisation numérique et expérimentale d'un secteur de virole en composite à matrice céramique soumis à des impacts

Nyssen Florence[1], Tableau Nicolas[2], Lavazec Déborah[2], Batailly Alain[1]

Résumé

Ce travail se focalise sur la caractérisation numérique et expérimentale des niveaux de contraintes au sein d'un secteur de virole fait d'un matériau composite à matrice céramique (CMC) soumis à des contacts d'aubes répétés. Le dispositif expérimental dédié consiste en un disque tournant, comportant trois aubes encochées qui impactent le secteur de virole en tournant. La plateforme sur laquelle le secteur est fixé se rapproche progressivement des aubes, de telle sorte que le revêtement abradable déposé sur la virole est progressivement usé à chaque révolution des aubes. Quatre capteurs, localisés sous le secteur de virole, sont utilisés pour mesurer les forces durant les tests expérimentaux. Différentes positions relatives de l'aube et du secteur sont testées, de telle sorte que les impacts se produisent à des positions distinctes sur le secteur. En plus des tests expérimentaux, un modèle numérique est construit, basé sur des modèles réduits de l'aube et du secteur de virole, dans le but de prédire numériquement les forces aux quatre capteurs. Tout d'abord, le modèle numérique est calibré sur un seul test expérimental de référence pour retrouver la même force à chaque capteur. Ensuite, les autres tests sont simulés en utilisant le modèle calibré. Les forces prédites sont en accord avec les données expérimentales, ce qui valide le modèle numérique. Finalement, les simulations sont menées en considérant des conditions moteur, qui ne pouvent pas être reproduite au moyen du banc d'essai. L'influence de plusieurs paramètres (la vitesse radiale, la position de l'impact, le nombre d'aubes en contact et la vitesse angulaire) sont analysées en détail.

Mots-clés

virole de turbine; composites à matrice céramique; impacts; interactions rotor-stator

1 - Département de génie mécanique, École Polytechnique de Montréal, P.O. Box 6079, Succ. Centre-Ville, Montréal, Québec, Canada H3C 3A7
2 - Safran Aircraft Engines, Villaroche, France

1 Introduction

In an increasingly competitive global market, aircraft engines manufacturers must design more efficient engines in order to reduce their fuel consumption both for economic and environmental reasons. Over the past decade, mainly two avenues have been considered to achieve this goal: (1) the use of novel and lighter materials [1] and, (2) the reduction of aerodynamic losses [2, 3], specifically in compressor stages [4, 5, 6].

The development of new materials—such as composite materials—has paved the way for significant mass reduction in aerospace structural components [1]. The use of such materials is indeed increasingly common for aircraft structures and even aircraft engines as they are typically found in the fan stage [7, 8], acoustic lining panels [9, 10, 11] as well as various components of the nacelle [12, 13]. However, the use of composite materials within the hot sections of an aircraft engine remains a challenge for engineers due to extreme thermal conditions. As a matter of fact, only few materials can provide satisfying mechanical performances when employed in the vicinity of the combustion chamber exhaust, such as the first turbine stages, where temperature may rise above $1,000°C$. Over the past years, researchers and engineers have worked on the use of ceramic matrix composites (CMC) materials in such areas, both for bladed components [14, 15, 16] and the surrounding static components [17, 18].

The second avenue considered by designers to increase an aircraft engine efficiency—the reduction of aerodynamic losses—implies a very stringent control of operating blade-tips/casings clearances in order to avoid any leak from higher to lower pressure stages. While a reduction of operating clearances provides a very significant improvement of the overall efficiency [19, 20, 21], it also unavoidably favors structural contacts between rotating and static components of the engine [22, 23]. Following such contact events, a variety of complex phenomena including blade failures [24], abnormal increases of temperature [25], and even modal interactions [26, 27] have been reported in the literature. This is the reason why the analysis and prediction of blade-tip/casing contact events have been a very active field of research over the past decade [28, 29, 30, 31, 32, 33, 34, 35, 36]. To this day, and to the best of the author's knowledge, the analysis of vibration phenomena subsequent to structural contacts in aircraft engines have essentially focused on compressor stages, where most significant efficiency improvements may be obtained by reducing clearances. Nonetheless, it is also important to ensure minimal clearances in turbine stages for better engine performances.

In this context, designing CMC static components in turbine stages—such as shroud segments—requires to account for structural contacts with rotating blade-tips that may occur in normal operating conditions. This is not an easy task as structural contacts induce nonlinear vibrations for which analysis strategies are scarce. Additionally, thermal effects and wear cannot be neglected thus requiring very costly numerical simulations that usually exceed the capabilities of commercial software packages. Yet, because CMC materials feature significantly lower admissible stresses than usual metal alloys, designers must accurately predict maximal stresses within CMC components in order to ensure an optimal lifespan. This motivates the development of multi-physics numerical *ad-hoc* strategies.

In this article, the focus is made on CMC shroud segments used in the turbine stages of an aircraft engine, see Fig. 1. The first section of the article presents an experimental set-up dedicated to the analysis of forces within a CMC shroud segment as it undergoes repeated contacts with a simplified mock blade. An abradable coating layer is

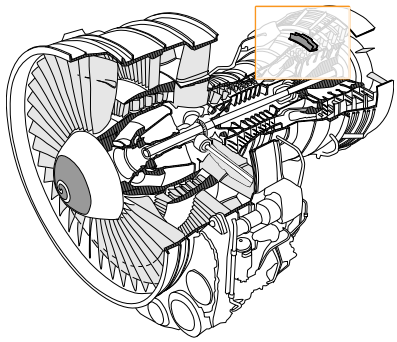

Figure 1. Schematic representation of a shroud segment within an aircraft engine.

deposited on the shroud segment in agreement with the actual engine configuration. Forces are measured at the back of the shroud segment for different contact configurations featuring varying incursion rates and contact locations.

Experimental results are then analyzed and compared to the outcomes of numerical simulations carried out with an evolution of an in-house numerical strategy [37]. Details and calibration of the numerical model are presented in the second section of the article. In the third section, the numerical model is carefully validated and particular attention is paid to its convergence with respect to key numerical parameters, such as the discretization of the contact surface and the numerical integration time step. Then, numerical results and experimental observations are thoroughly compared in the fourth section. Finally, in the fifth section, the numerical model is used to predict the vibration behaviour of the analyzed CMC shroud segment when impacted by the actual turbine blade considering engine-like operating conditions.

2 Experimental investigations

2.1 Description of the experimental set-up

The experimental set-up consists in a simplified rotor with three identical mock blades notched in a rotating disk. A schematic representation of the experimental set-up is shown in Fig. 2a, and a picture of the test bench is given in Fig. 2b, in which the shroud segment has been blured for the sake of confidentiality. A high speed recording camera (model: PHOTRON SA4 RV) is located in front of the test set-up focusing on the contact area, see Fig. 3. During each test, the disk rotates at a constant angular speed denoted Ω. The three mock blades feature a short height and width compared to an actual engine blade, thus making them very stiff. This ensures that blades' vibrations will be negligible throughout the interaction to keep the focus on the shroud segment's vibration behaviour.

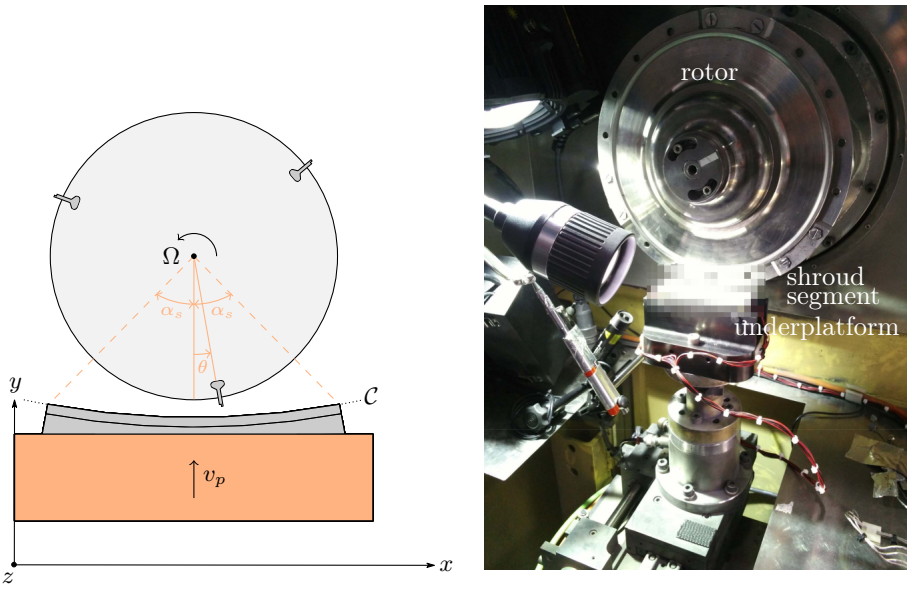

(a) schematic representation **(b)** real test bench

Figure 2. Experimental set-up.

The CMC shroud segment of interest, an actual engine component, is located below the rotor. The CMC shroud segment is approximately 10 cm long. It is made of a SiC/SiC composite, and its abradable layer is composed of rare-earth element-based disilicate. It is held by two clamping jaws and supported in four points, see Fig. 4. Four subminiature load buttons (model: Futek LLB130 FSH02950) located at the back of the shroud segment—at positions A, B, C and D shown in Fig. 4—allow to measure the forces applied by the shroud segment as the

Figure 3. High speed recording camera

interaction occurs. The rig with the shroud segment can translate along the $+y$ direction with a constant velocity, denoted v_p. Based on empirical observations, a single value of v_p will be considered experimentally. An abradable coating layer is deposited along the shroud segment contact surface. As the shroud segment translates towards the rotor, blades/shroud contacts occur thus yielding both abradable material removal and significant stress levels within the shroud segment. The rotor's radius of curvature is smaller than the shroud one (see the circular arc $\mathcal{C}$ in Fig. 2 that follows the shroud segment curvature) in order to ensure a localized contact area and to avoid contacts in the vicinity of the outer edges of the shroud segment. The rig with the shroud segment can also translate along the x and z directions such that the blade can impact the shroud segment at different locations.

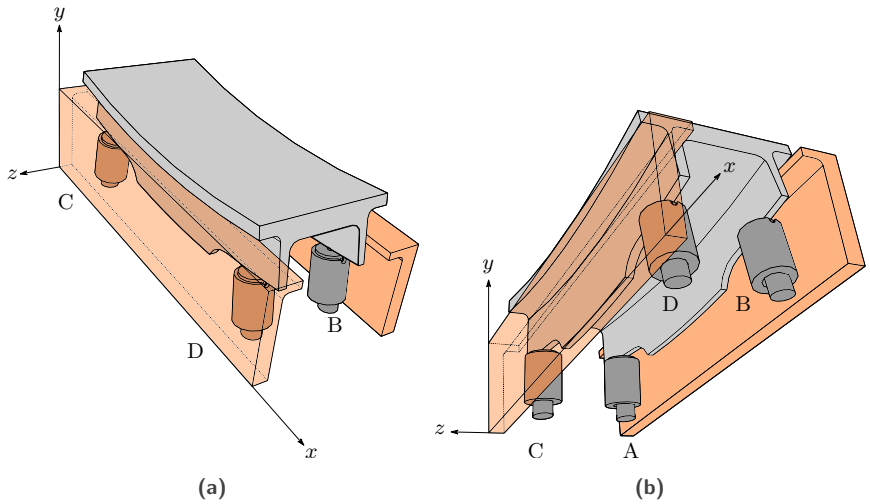

Figure 4. Shroud segment and the four force sensors, (a) upper view and (b) bottom view.

2.2 Different contact scenarios

Various positions of the shroud segment in the (x, z) plane may be considered in order to test different contact areas. In total, five distinct contact areas are considered experimentally, they are denoted $c_i,\ i = 1, \ldots, 5$ in Fig. 5. Contact area c_1 is located at the center of the shroud segment's contact surface. Areas c_2 and c_4 are centered with respect to the z direction. Remaining contact areas c_3 and c_5 are purposely located closer to a single force sensor—respectively B and C—in order to generate asymmetric interactions.

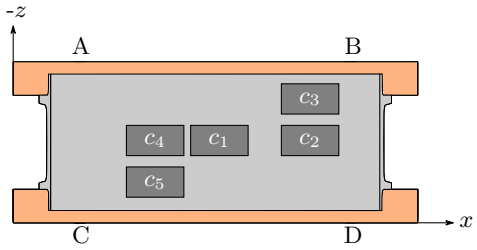

Figure 5. Contact locations c_i for each test configuration.

2.3 Experimental parameters

The disk angular speed Ω remains constant along the test duration. Due to technical limitations, the velocity is equal to 85 % of the nominal engine angular velocity. Tests are conducted at room temperature T. An abradable layer of thickness e_{ab} is deposited onto the shroud segment. The shroud segment moves towards the rotor at the constant velocity v_p, and the targeted wear depth at the end of the test is noted p. The damping of the first two modes of the shroud segment has been characterized with ping tests. The mock blades used in the test bench has a short length and height compared to the engine blade.

2.4 Treatment of acquired signals

The signal at each force sensor has been acquired at a frequency > 250 kHz, which ensure to capture the dynamical responses of the system. Specific numerical procedures based on the cyclo-non-stationary method are developed by Safran in order to filter the time responses obtained for each interaction test from sensors A, B, C and D. An extensive presentation of this procedure goes beyond the scope of this article, the reader may refer to [38] for more details about it.

2.5 Experimental results

For the sake of confidentiality, all experimental measurements presented in this section are normalized both in time and amplitude.

2.5.1 Force signals for c_1

Force signals obtained at each sensor for interaction configuration c_1 are pictured in Fig. 6. $t = 0$ corresponds to the blades/shroud segment first contact. The shroud segment moves towards the rotor between $t = 0$ and $t = 1$. For $t > 1$, the shroud segment stops moving towards the rotor, some remaining decreasing contact forces are measured at sensors A, B, C, and D. $t_{25\%}$ refers to the last peak value in the contact force signals over $t \in [0; 0.25]$. For each configuration, there are more than $1,500$ contact events during the whole test. Accordingly, the envelope of force signals depicted in Figs. 6a, 6b, 6c and 6d essentially underlines the evolution of the maximum force measured by each sensor during the interaction. Additionally, a linear regression based on the peak values obtained for $t \in [0,\ t_{25\%}]$ is plotted in black (——) in each plot.

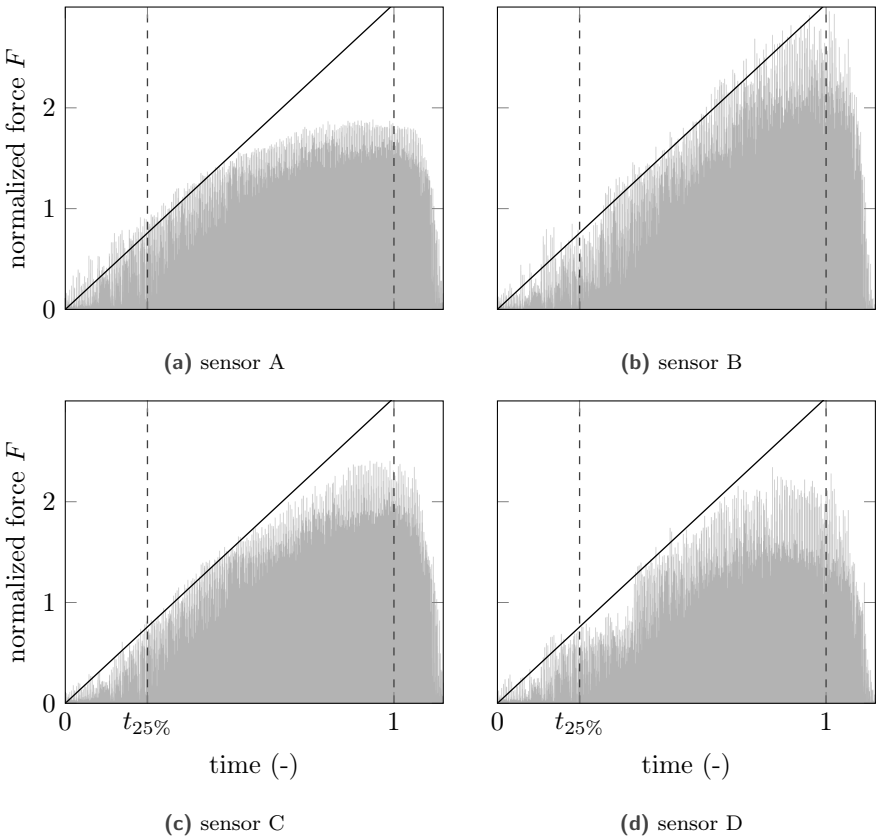

(a) sensor A **(b)** sensor B

(c) sensor C **(d)** sensor D

Figure 6. Force signals obtained for configuration c_1.

While contact area c_1 is centered on the shroud segment, there is a distinct evolution of measured forces on each sensor with respect to time. Relative forces measured on each sensor at $t = t_{25\%}$ and $t = 1$ are depicted in Fig. 7. It

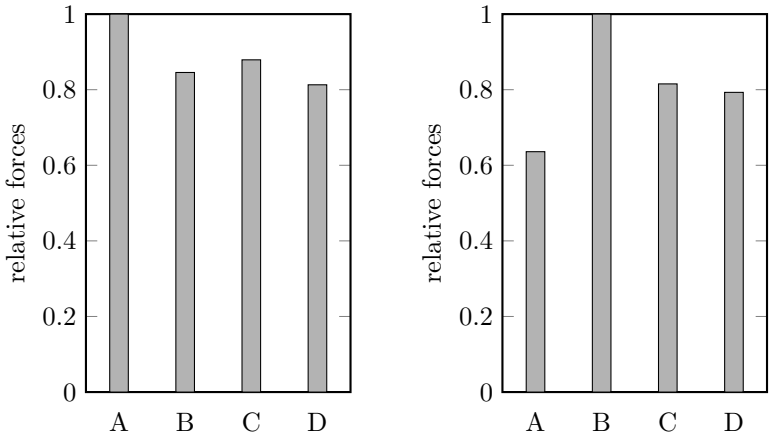

(a) $t = t_{25\%}$ **(b)** $t = 1$

Figure 7. Configuration c_1: distribution of measured forces.

is noticeable that the maximum variation of measured forces from a sensor to another is 19 % at $t = t_{25\%}$ while it reaches up to 38 % at $t = 1$. This observation is consistent with the fact that contact forces measured by sensors A, C and D do not follow the trend established from the first 25 % of the test. The use of the high speed recording camera focusing on the contact area provides additional insight on the nature of the interaction. For $t > t_{25\%}$, as the abradable coating is repeatedly impacted, it is noticeable that the color of the contact area changes and becomes bright orange (see Fig. 8), indicating a very significant heating of the area. From that point, it is assumed that thermal effects strongly impact the nature of the interaction and two phases may be distinguished:

$t < t_{25\%}$: the interaction essentially involves both structural dynamics and wear, the abradable coating is progressively worn out and the shroud segment vibrates under repeated impact loadings,

$t \geq t_{25\%}$: the contribution of thermal effects imply a much more sophisticated interaction where increases of temperature yields a combination of shroud segment vibrations, abradable coating wear, blade wear and thermal expansions.

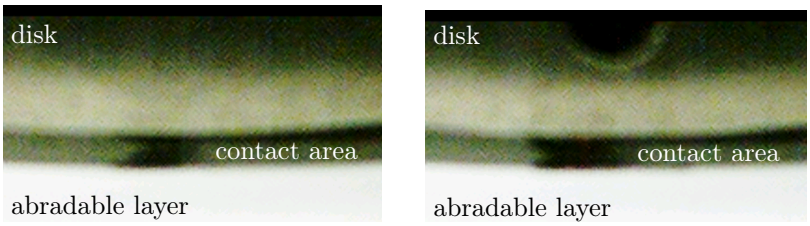

(a) $t \simeq 0.1$ **(b)** $t \simeq t_{25\%}$

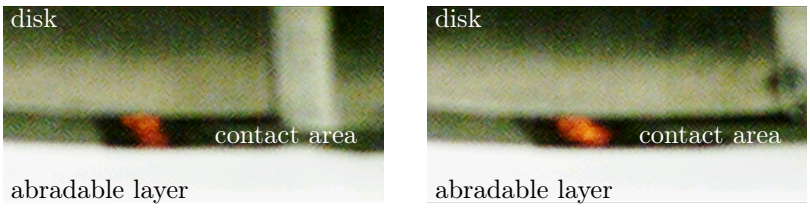

(c) $t \simeq 0.5$ **(d)** $t \simeq 1$

Figure 8. Picture of contact area from the high speed camera at different moments.

As a first approach, the remainder of the article focuses on values obtained at $t = t_{25\%}$ in order to put aside the contribution of thermal effects. This decision is motivated by the fact that experimental observations suggest that thermal effects yield a reduction of measured contact forces. For this reason, it is assumed that putting aside thermal effects will provide, as a first approximation, a conservative estimation of maximal stresses within the shroud segment.

2.5.2 Measured forces at $t = t_{25\%}$

The distribution of measured forces on each sensor at $t = t_{25\%}$ is given for each contact configuration in Fig. 9. These results are to be analyzed in light of the location of each contact configuration, see Fig. 5. In agreement with the location of each contact area c_i, measured forces may be symmetric or not. For instance, contact configuration c_2 which is shifted along the x direction towards sensors B and D logically corresponds to higher measured forces on these sensors. Similarly, contact configurations c_3 and c_5, respectively located close to sensors B and C, yield maximum contact forces on these sensors.

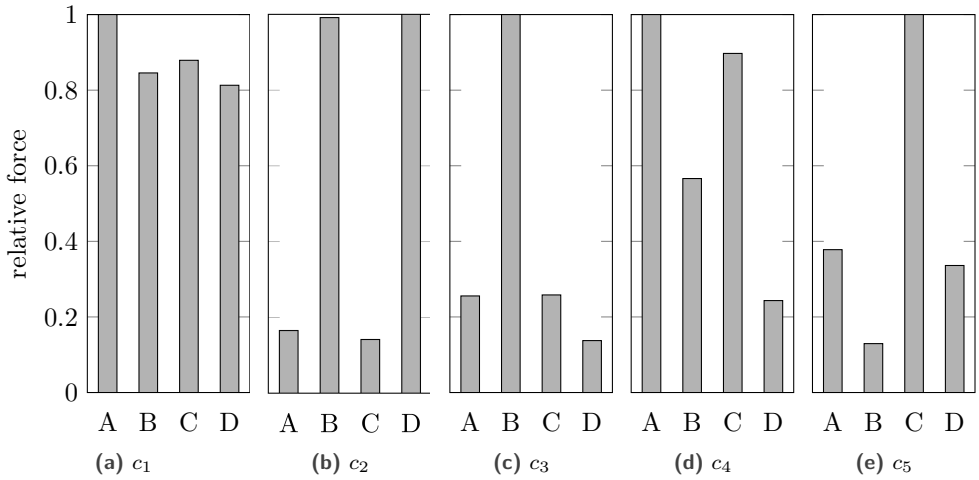

(a) c_1 **(b)** c_2 **(c)** c_3 **(d)** c_4 **(e)** c_5

Figure 9. Distribution of measured forces for each contact configuration at $t = t_{25\%}$.

2.5.3 Components wear

The significant contribution of thermal effects leads to wear on both the blades and the abradable coating at the end of each test. A picture of the three blades tips at the end of test case c_1 is shown in Fig 10. Stripes are observed on all blades, which indicate significant wear. Also, the profilometry of the shroud segment's contact area at the end of c_1 in Fig. 11 shows a cavity of depth p.. Wear levels measured on the blades (the mean value of the wear

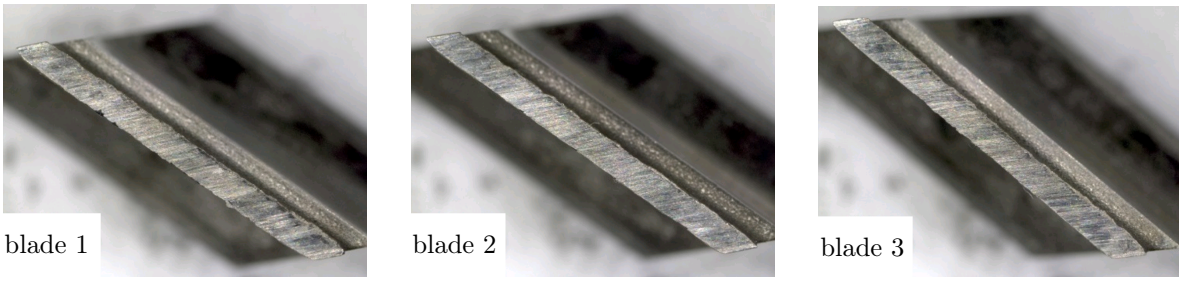

(a) **(b)** **(c)**

Figure 10. Blades wear at the end of test case c_1: (a) blade 1, (b) blade 2, and (c) blade 3.

observed on each blade is here reported) and the abradable coating at the end of tests conducted for each contact configuration are summed up in Fig. 12. Values are normalized with respect to the targeted wear depth p. Significant levels of blade wear are evidenced. As a consequence, abradable wear is lower than the targeted value p.

2.6 Summary of the experimental investigations

Experimental observations underline that the simulated interactions are inherently multi-physical as structural dynamics, abradable wear, blade wear and thermo-mechanics are entangled. For all contact configurations however, it is evidenced that thermal effects seem negligible over the first 25% of the interaction: no high temperatures have been recorded over $t \in [0; t_{25\%}]$.. Thus, over this period of time, the different contact configurations tested on the experimental set-up provide useful data for the calibration of a numerical strategy which accounts for abradable wear and structural dynamics. As is, the experimental set-up does not allow for tests featuring engine-like conditions: tests are carried out at room temperature, the rotor speed is slightly lower that the actual engine and the rotor

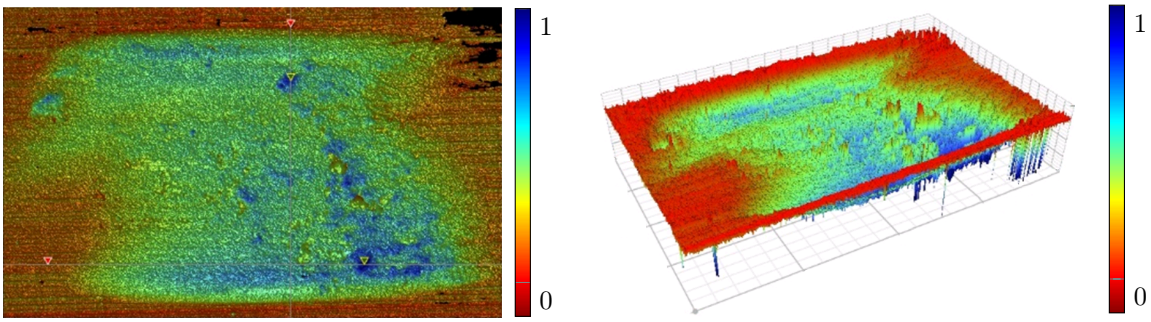

(a) top view **(b)** perspective view

Figure 11. Wear morphology at the end of test case c_1.

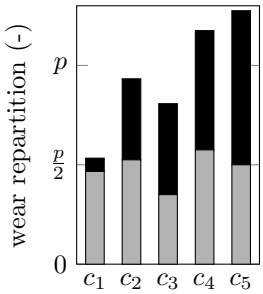

Figure 12. Normalized blade (■) and abradable layer's (■) wear distribution at the end of each experimental test case.

diameter is smaller than the considered turbine stage. However, it is advantageously much less costly than operating a full scale turbine stage and may easily be used for other types of shroud segments and static components subjected to contact events.

3 Numerical strategy

The presented numerical strategy relies on an in-house tool dedicated to the prediction of blade-tip/casing contact interactions [30]. Previous work carried out with this methodology usually involved a perfectly rigid casing in order to focus on the blade vibration response. This numerical strategy is here extended to segmented flexible stator components building on previous developments presented in [37] for full 360° casings.

3.1 Modeling

3.1.1 Blade

The mock blade finite element model is reduced using the Craig-Bampton-based reduction technique detailed in [30] which yields the reduced mass, damping and stiffness matrices of a blade, respectively $\mathbf{M}_b$, $\mathbf{D}_b$ and $\mathbf{K}_b$. The degrees of freedom retained in the reduced model are those of nodes located along the blade chord in order to allow efficient contact treatment, see the 9 retained nodes along the blade tip evidenced in red in Fig. 13. Nodes that are in contact with the disk during the interaction are numerically clamped, see dark gray area and clamped nodes in blue in Fig. 13. The reduction parameter η_b of this model—the number of constraint modes retained in the reduction basis—is found to have low to no effect on the numerical simulations due to the very large stiffness of the mock blades. In the following, $\eta_b = 100$. It has been checked that increasing η_b has no noticeable impact on the presented results.

Because only one blade is modeled instead of 3 as in the experimental set-up, simulations are carried out at

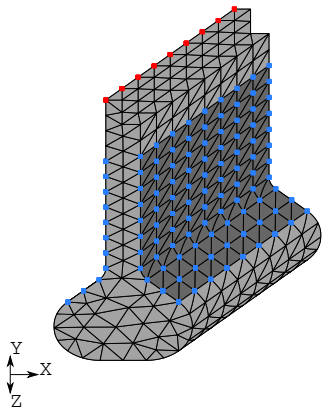

Figure 13. Mock blade finite element model, retained nodes in red (●) and clamped nodes in blue (●).

a blade angular speed equal to 3 times the experimental angular speed in order to excite the shroud segment at the same frequency than in the experiments. Due to the small blade height—a few millimeters only—and its high rigidity, centrifugal loads have low effects and are neglected for the mock-up blade. In this context, the blade angular speed can be tripled whithout overestimating its centrifugal displacement.

3.1.2 Shroud segment

The finite element model of the CMC shroud segment cannot be shown for the sake of confidentiality. The finite element model of the shroud is built on the geometry shown in Fig. 14. It is made of 76, 604 nodes and 60, 581 linear finite elements. The shroud segment is clamped in front of the four sensor locations.

Managing contact between the blades and the shroud segment requires a continuous definition of the normal vector to the contact surface as the blades rotate. This prevents a definition of the normal vector that would rely on finite elements [37]. For this reason, a bi-cubic B-spline surface is computed over the shroud segment contact surface. This surface relies on a few selected nodes, see Fig. 14. The role of the B-spline surface, as introduced in [37], is threefold: (1) it provides a support for the definition of a smooth normal vector along the contact surface, (2) it allows to compute blade/segment distances for each contact node of the mock blades and, (3) it is used to distribute contact forces on the shroud segment when it is impacted by a mock blade.

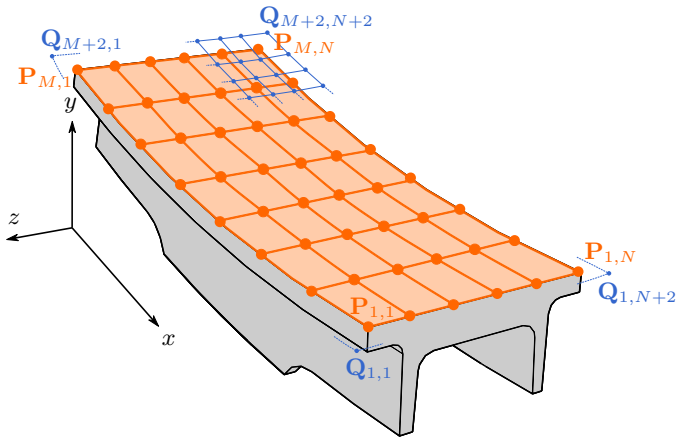

Figure 14. Contact surface of the shroud segment and retained nodes $\mathbf{P}_{i,j}$ and control points $\mathbf{Q}_{i,j}$.

For the sake of efficacy, the finite element model of the shroud segment is reduced by means of the Craig-Bampton [39] reduction technique where retained boundary nodes are those used for the computation of the B-spline

surface. This yields the reduced mass, damping and stiffness matrices of a shroud segment, respectively $\mathbf{M}_s$, $\mathbf{D}_s$ and $\mathbf{K}_s$.

3.1.3 B-spline calculation

Free boundary conditions are imposed along edges of the B-spline surface. For the sake of clarity, equations are written in matrix form using vectors $\mathbf{P}$ and $\mathbf{Q}$ that concatenate all data points and control points such as:

$$\mathbf{P} = \begin{pmatrix} \mathbf{P}_{1,1} \\ \mathbf{P}_{2,1} \\ \vdots \\ \mathbf{P}_{N,M} \end{pmatrix}, \qquad \mathbf{Q} = \begin{pmatrix} \mathbf{Q}_{1,1} \\ \mathbf{Q}_{2,1} \\ \vdots \\ \mathbf{Q}_{N,M} \end{pmatrix} \tag{1}$$

The control points $\mathbf{Q}_n$ used to build the spline surface at a time step n can be computed based on the data points $\mathbf{P}_n$, which correspond to the shroud boundary nodes' coordinates at time step n, using:

$$\mathbf{Q}_n = \mathbf{C}\left(\mathbf{AC}\right)^{-1}\mathbf{P}_n \tag{2}$$

where the matrix $\mathbf{C}$ is related to the boundary conditions imposed on the spline surface—free-edges here—and $\mathbf{A}$ is the interpolation matrix. The spline surface, and therefore the control points $\mathbf{Q}_n$, are updated with the displacement of shroud boundary nodes. Matrices $\mathbf{C}$ and $\mathbf{A}$ are independent of the data points coordinates $\mathbf{P}_n$ and can be computed ones. The mathematical formulation of matrix $\mathbf{A}$ can be found in [37]. The expression of matrix $\mathbf{C}$ accounts for free-edge boundary conditions. For control points at each corner (see Fig. 14), the symmetry conditions can be written as [40]

$$\mathbf{Q}_{1,1} = 2\mathbf{Q}_{2,2} - \mathbf{Q}_{3,3} \tag{3}$$
$$\mathbf{Q}_{1,M+2} = 2\mathbf{Q}_{2,M+1} - \mathbf{Q}_{3,M} \tag{4}$$
$$\mathbf{Q}_{N+2,1} = 2\mathbf{Q}_{N+1,2} - \mathbf{Q}_{N,3} \tag{5}$$
$$\mathbf{Q}_{N+2,M+2} = 2\mathbf{Q}_{N+1,M+1} - \mathbf{Q}_{N,M} \tag{6}$$

Along each of the four edges of the spline, free-edge boundary conditions are written as follows:

$$\mathbf{Q}_{1,j} = 2\mathbf{Q}_{2,j} - \mathbf{Q}_{3,j}, \qquad j = [2, 3, \ldots, M+1] \tag{7}$$

$$\mathbf{Q}_{i,1} = 2\mathbf{Q}_{i,2} - \mathbf{Q}_{i,3}, \qquad i = [2, 3, \ldots, N+1] \tag{8}$$

$$\mathbf{Q}_{i,M+2} = 2\mathbf{Q}_{i,M+1} - \mathbf{Q}_{i,M}, \qquad i = [2, 3, \ldots, N+1] \tag{9}$$

$$\mathbf{Q}_{N+2,j} = 2\mathbf{Q}_{N+1,j} - \mathbf{Q}_{N,j}, \qquad j = [2, 3, \ldots, M+1] \tag{10}$$

These two sets of conditions lead, in matrix form, to the following expression of the $\mathbf{C}$ matrix:

$$\mathbf{C} = \begin{bmatrix}
2 & 0 & \dots & 0 & -1 & 0 & 0 & 0 & \dots & 0 & 0 & 0 & 0 \\
2 & 0 & \dots & 0 & -1 & 0 & 0 & 0 & 0 & \dots & 0 & 0 & 0 \\
2 & 0 & 0 & \dots & 0 & -1 & 0 & 0 & 0 & \dots & 0 & 0 & 0 \\
\vdots & & & & & & \ddots & & & & & & \vdots \\
0 & \dots & 0 & 2 & 0 & \dots & 0 & -1 & 0 & 0 & \dots & 0 & 0 \\
2 & -1 & 0 & 0 & 0 & 0 & 0 & \dots & 0 & 0 & 0 & 0 & 0 \\
1 & 0 & 0 & 0 & 0 & 0 & \dots & 0 & 0 & 0 & 0 & 0 & 0 \\
0 & 1 & 0 & 0 & 0 & 0 & \dots & 0 & 0 & 0 & 0 & 0 & 0 \\
\vdots & & & & & & \ddots & & & & & & \vdots \\
0 & \dots & 0 & -1 & 2 & 0 & 0 & 0 & 0 & \dots & 0 & 0 & 0 \\
0 & 0 & \dots & 0 & 0 & 2 & -1 & 0 & 0 & \dots & 0 & 0 & 0 \\
0 & 0 & \dots & 0 & 0 & 1 & 0 & 0 & 0 & \dots & 0 & 0 & 0 \\
0 & 0 & \dots & 0 & 0 & 0 & 1 & 0 & 0 & \dots & 0 & 0 & 0 \\
\vdots & & & & & & \ddots & & & & & & \vdots \\
0 & 0 & 0 & \dots & 0 & -1 & 2 & 0 & 0 & 0 & \dots & 0 & 0 \\
0 & 0 & 0 & \dots & 0 & 0 & 0 & 2 & -1 & 0 & \dots & 0 & 0 \\
0 & 0 & 0 & \dots & 0 & 0 & 0 & 1 & 0 & 0 & \dots & 0 & 0 \\
0 & 0 & 0 & \dots & 0 & 0 & 0 & 0 & 1 & 0 & \dots & 0 & 0 \\
\vdots & & & & & & \ddots & & & & & & \vdots \\
0 & 0 & 0 & 0 & 0 & \dots & 0 & 0 & 0 & 0 & 0 & -1 & 2 \\
0 & 0 & \dots & 0 & -1 & 0 & \dots & 0 & 2 & 0 & 0 & \dots & 0 \\
0 & \dots & 0 & -1 & 0 & 0 & \dots & 0 & 2 & 0 & 0 & \dots & 0 \\
0 & \dots & 0 & 0 & -1 & 0 & 0 & \dots & 0 & 2 & 0 & \dots & 0 \\
\vdots & & & & & & \ddots & & & & & & \vdots \\
0 & 0 & 0 & \dots & 0 & 0 & 0 & -1 & 0 & \dots & 0 & 2 & 0 \\
0 & 0 & 0 & \dots & 0 & 0 & 0 & 0 & -1 & 0 & \dots & 0 & 2 \\
0 & 0 & 0 & \dots & 0 & 0 & 0 & -1 & 0 & \dots & 0 & 0 & 2
\end{bmatrix} \tag{11}$$

The relative blade/shroud velocity v_p along the radial direction is constant. It is imposed on the B-spline surface in agreement with the displacement of the underplatform in the experimental set-up.

3.2 Blade/shroud distances computation

As the blade rotates, two distinct phases can be distinguished, as can be seen in Fig. 2: (1) in a limited angular sector in front of the shroud segment—*i.e.* $\theta \in [-\alpha_s, \alpha_s]$ where $2\alpha_s$ defines the shroud segment angular sector, see Fig. 2—, the blade may enter in contact with the shroud segment thus nonlinear simulations are required, while (2) outside of the angular sector, both components vibrate linearly as contact can not occur.

The computation of blade/shroud distances in the angular sector $\theta \in [-\alpha_s, \alpha_s]$ is done using the procedure detailed in [37]. An iterative Newton-Raphson procedure is employed to compute the closest point to each blade boundary node on the spline contact surface at the n^{th} time step. The starting point of the iterative procedure is the location of the closest point at the previous time step $n-1$. The stop criterion of the Newton-Raphson procedure is set to 10^{-10} in order to ensure convergence.

3.3 Equation of motion

The reduced equation of motion of the blade/shroud segment system reads:

$$\begin{bmatrix} \mathbf{M}_b & \mathbf{0} \\ \mathbf{0} & \mathbf{M}_s \end{bmatrix} \begin{bmatrix} \ddot{\mathbf{u}}_b \\ \ddot{\mathbf{u}}_s \end{bmatrix} + \begin{bmatrix} \mathbf{D}_b & \mathbf{0} \\ \mathbf{0} & \mathbf{D}_s \end{bmatrix} \begin{bmatrix} \dot{\mathbf{u}}_b \\ \dot{\mathbf{u}}_s \end{bmatrix} + \begin{bmatrix} \mathbf{K}_b(\Omega) & \mathbf{0} \\ \mathbf{0} & \mathbf{K}_s \end{bmatrix} \begin{bmatrix} \mathbf{u}_b \\ \mathbf{u}_s \end{bmatrix} + \begin{bmatrix} \mathbf{F_c}(\mathbf{u_b}) \\ \mathbf{F_c}(\mathbf{u_s}) \end{bmatrix} = \begin{bmatrix} \mathbf{0} \\ \mathbf{0} \end{bmatrix} \tag{12}$$

where $\mathbf{u}_b$ and $\mathbf{u}_s$ denote the reduced blade and shroud displacements. Ω is the angular velocity. $\mathbf{F}_c(\mathbf{u}_b)$ contains the contact forces at the blade tip, and $\mathbf{F}_c(\mathbf{u}_s)$ the contact forces at the shroud segment boundary nodes. No external force is considered.

3.4 Abradable coating and wear

The abradable layer is modeled as 2-node bar elements, governed by a elasto-plastic constitutive law described in [30], deposited onto the shroud segment. To avoid unnecessary computation times, the abradable layer's mesh

has the same width than the blade, as illustrated in Fig. 15. The abradable coating is discretized by means of N_{ab} evenly spaced elements along the shroud segment circumferential direction, and N_b—the number of boundary nodes in the blade reduced order model (ROM)—elements along the axial direction.

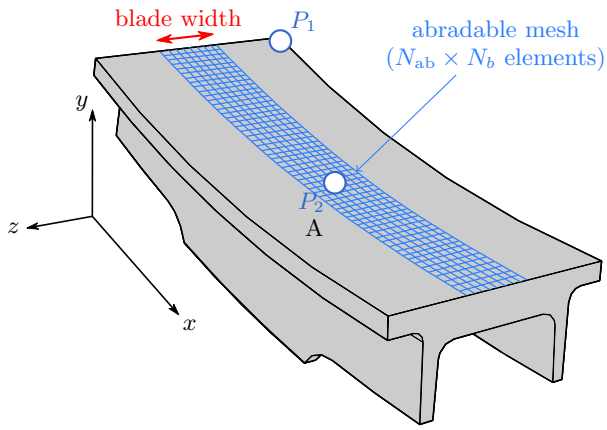

Figure 15. Abradable layer's mesh.

Potential penetration of the blade within the abradable coating is assessed by the computation of the distance of each blade boundary node to the spline surface along the shroud segment. If a penetration is detected for a blade boundary node, a contact force is computed and the abradable layer is worn. The abradable wear is modeled as a plastic deformation of the impacted abradable elements $\Delta\varepsilon_p^n$—the computation of this term depending on the contact forces is extensively detailed in [30]—, such that the local thickness of the abradable at time step n is $e_{\text{ab}}^n = e_{\text{ab}}^{n-1} - \Delta\varepsilon_p^n$.

3.5 Contact treatment and time integration

The equation of motion of the blade and the shroud segment, see Eq. (12), is solved using an explicit central finite difference time integration scheme [30]. The flow chart that summarizes the time integration procedure is given in Fig. 16:

displacement prediction: Blade and shroud displacements at time step $n+1$, denoted $\mathbf{u}_{b,n+1}^\star$ and $\mathbf{u}_{s,n+1}^\star$, are first predicted using their displacements at the two previous time steps n and $n-1$. The $\star$ symbol refers to predicted quantities.

spline update: The coordinates of spline data points $\mathbf{P}_{n+1}^\star$ are updated based on the shroud displacement predictions $\mathbf{u}_{s,n+1}^\star$ and on the shroud's radial velocity v_p. The notation $\mathbb{1}$ in Fig. 16 refers to a column vector of 1. Based on the updated data points $\mathbf{P}_{n+1}^\star$, control points at time step $n+1$, $\mathbf{Q}_{n+1}^\star$, are computed to update the B-spline surface.

distance computation: If the blade is located in the angular sector of the shroud segment, *i.e.* $\theta \in [-\alpha_s, \alpha_s]$, the distance between the blade and the shroud, noted $\mathbf{d}_{n+1}^\star$, is evaluated using the updated B-spline.

contact and wear: If a contact with the abradable layer is detected—meaning that the distance $\mathbf{d}_{n+1}^\star$ between one blade boundary node and the updated B-spline surface is negative—, the blade and shroud contact matrices $\mathbf{C}_{b,n+1}^{\text{ab}}$ and $\mathbf{C}_{s,n+1}^{\text{ab}}$ are computed, as well as the contact forces $\boldsymbol{\lambda}_{n+1}^{\text{ab}}$. Based on these contact forces, abradable layer's wear $\Delta\varepsilon_p^{n+1}$ is evaluated for the impacted elements.

displacement correction: The blade and shroud displacements are then corrected such that the distance between the shroud and the blade boundary nodes in contact is zero to avoid interpenetration of the two components.

linear simulation: If the blade is located outside of the angular sector of the shroud, *i.e.* $\theta \notin [-\alpha_s, \alpha_s]$, displacement predictions, $\mathbf{u}_{b,n+1}^\star$ and $\mathbf{u}_{s,n+1}^\star$, are admissible and no correction is required.

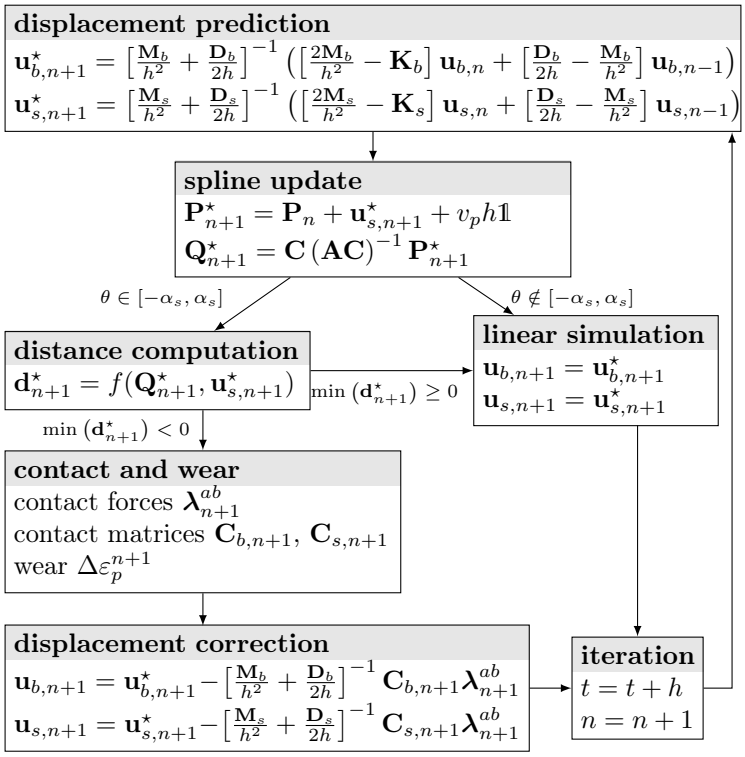

Figure 16. Flow chart of the time integration scheme with abradable layer's wear treatment.

3.6 Computation of force signals at each sensor

The comparison between numerical results and experimental observations focuses on one specific quantity of interest: the time evolution of radial forces as measured by sensors A, B, C and D, see orange arrows in Fig. 17. The outputs of the time integration scheme detailed in section 3.5 are the reduced blade and shroud displacements $\mathbf{u}_b$ and $\mathbf{u}_s$, at each time step. Therefore, additional computations are needed to evaluate the force signals at each sensor based on the reduced displacements.

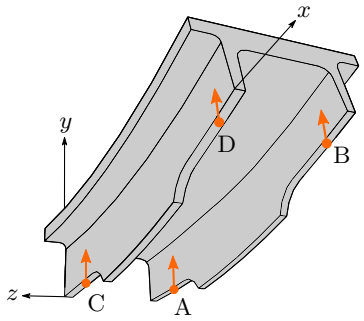

Figure 17. Forces of interest at the four sensors.

First, the projection of the reduced shroud displacements in the full finite element mesh allows to retrieve the physical displacement field for all mesh nodes at each time step. Then, using this physical displacement field, the stress field within the full structure can be evaluated, as well as the forces in the shroud. By restricting the stress computation to A, B, C and D areas—that correspond to the clamping conditions of the finite element model—in the radial direction, the force signals at each sensor can be numerically obtained. These results can be directly

compared with the experimental signals.

The assumption made in the numerical model of clamping conditions at the sensors location is an idealization of the actual boundary conditions. In the experiments, shroud segment/sensors contacts occur only for negative y displacements. For positive y displacements, there is no contact between the shroud segment and the force sensors. The clamping conditions can induce differences between numerical and experimental results. The shape of clamping areas are also approximated in the numerical model: simplified rectangular clamping areas are considered in the model.

4 Convergence and validation

It is not possible to obtain a reference solution with full finite element models. Indeed, such computations would yield excessively long computation times. For that reason, this section focuses on the asymptotic convergence of the numerical procedure as the accuracy of the employed models is increased using, for instance, finer space discretization or richer modal reduction bases. Simulations for the convergence analysis are performed on the c_1 configuration, *i.e.* with an impact location centered on the shroud segment, focusing on the first contact event. All results are normalized for the sake of confidentiality.

4.1 Time convergence

Convergence of the numerical procedure is first assessed with respect to the time step of the time integration procedure. On one hand, the use of an explicit scheme typically implies very small time steps—usually in the vicinity

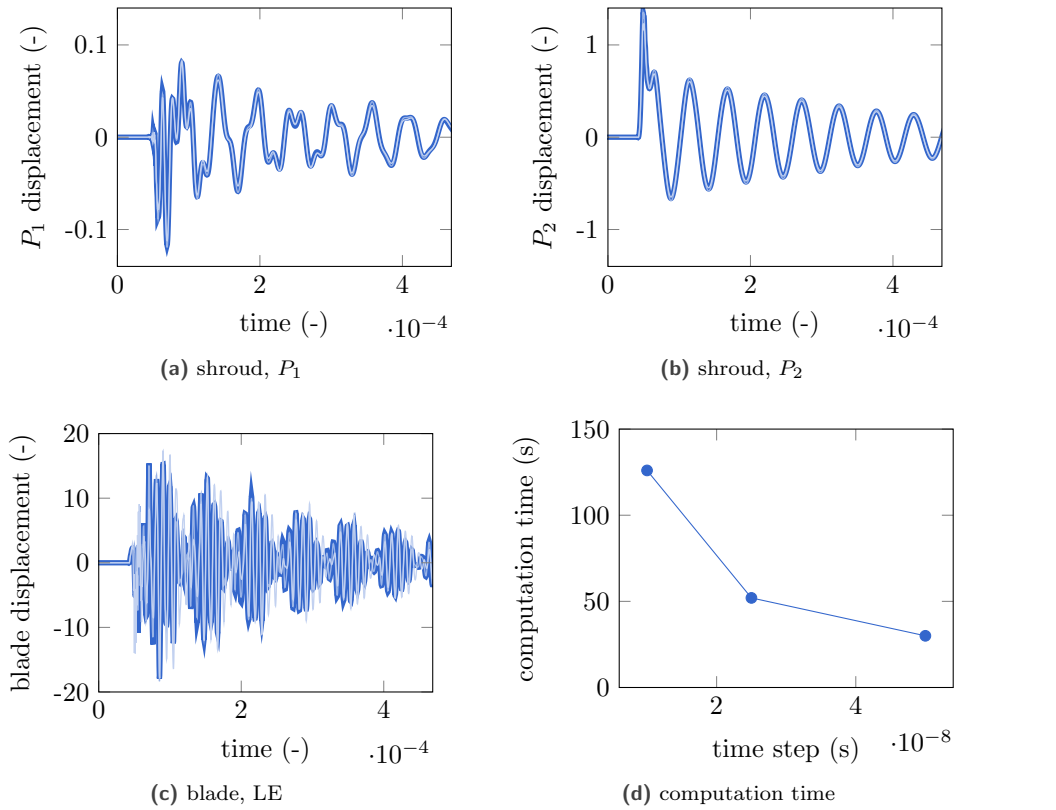

(a) shroud, P_1 **(b)** shroud, P_2

(c) blade, LE **(d)** computation time

Figure 18. Convergence with the time step: $h = 5 \cdot 10^{-8}$ s (——), $h = 2.5 \cdot 10^{-8}$ s (——), $h = 10^{-8}$ s (——).

of $h = 10^{-7}$ s—which may lead to significant computation times. On the other hand, such time integration scheme advantageously allows to assume a linear evolution of displacement fields from a time step to another which is fast

to compute. For the simulation of experimental tests, finer time steps of $5 \cdot 10^{-8}$ s or less must be considered to ensure stable computations due to the high eigenfrequencies of the blade and the shroud segment. For each of these values, the time response of the radial displacement computed at three distinct locations are plotted in Fig. 18: the radial displacement of point P_1 on the shroud segment in Fig. 18a, the radial displacement of point P_2 on the shroud segment in Fig. 18b and the radial displacement of the blade's leading edge contact node in Fig. 18c. The reader may refer to Fig. 15 for the location of each point P_i. Computation times associated with each simulation, conducted on a standard $i7$-processor computer, are summarized in Fig. 18d.

Plots corresponding to shroud segment's radial displacements, see Figs. 18a and 18b, rapidely converged when reducing the time step h. Considering $h = 5 \cdot 10^{-8}$ s allows to accurately capture the shroud dynamics. However, for the blade displacements, see Fig. 18c, the curve obtained with $h = 5 \cdot 10^{-8}$ s (——) differs from the ones related to lower h values. Smaller time steps are therefore required to accurately describe blade displacements. This can be explained by the high blade stiffness: only a few millimeters at blade tip are indeed free to vibrate due to its boundary conditions, which leads to high blade eigenfrequencies. Because the focus of the work relies on shroud dynamics and the computation times increase rapidly as the time step is refined, see Fig. 18d, a time step of $5 \cdot 10^{-8}$ s is considered in the following, which is sufficient to accurately predict shroud displacements while ensuring efficient numerical simulations.

4.2 Space convergence

4.2.1 Reduction parameter

Convergence of simulation results is analyzed with respect to the reduction parameter η_s, which corresponds to the number of modes retained in the shroud ROM. Because contact events may yield the participation of potentially

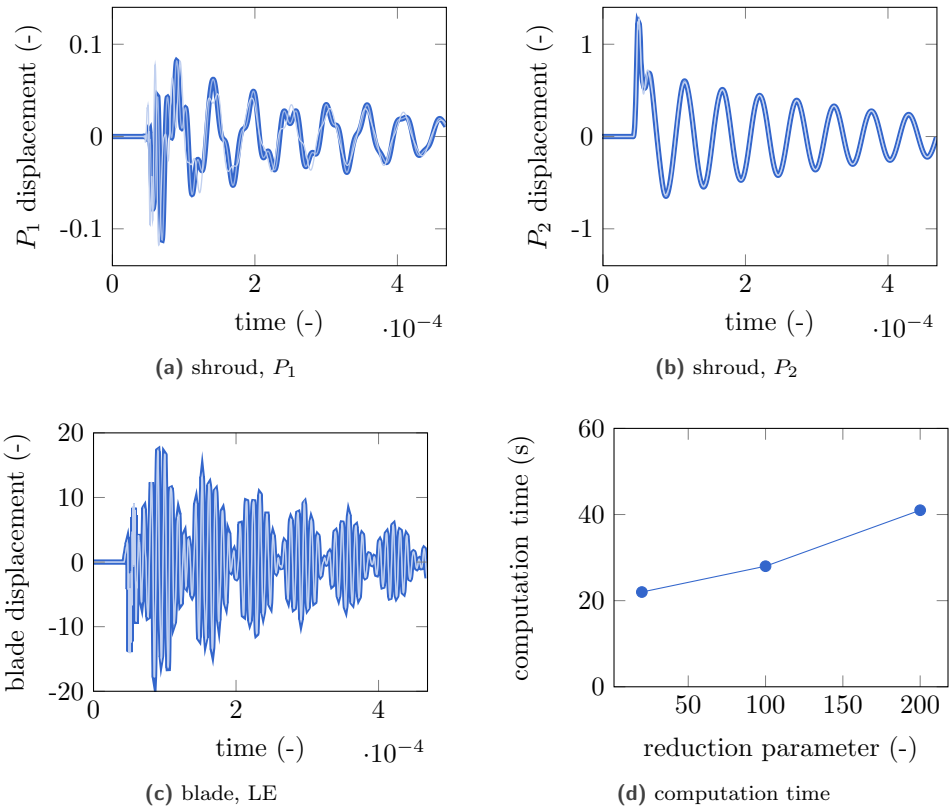

(a) shroud, P_1 **(b)** shroud, P_2

(c) blade, LE **(d)** computation time

Figure 19. Convergence with the reduction parameter: $\eta_s = 20$ (——), $\eta_s = 100$ (——), $\eta_s = 200$ (——).

high-frequency free-vibration modes, a large number of modes are needed in the ROM to accurately describe the displacements. Simulations are carried out with three different values of η_s: 20, 100 and 200. Associated radial displacement at point P_1 on the shroud segment for the three η_s values is shown in Fig. 19a, the radial displacement at point P_2 in Fig. 19b, and the radial displacement at the blade leading edge in Fig. 19c.

In Fig. 19a, the curve obtained for $\eta_s = 20$ stands out, it differs from the ones obtained with $\eta_s = 100$ and $\eta_s = 200$, which are superimposed. In Fig. 19b, the curve $\eta_s = 20$ slightly differs from the two other curves. Results obtained with $\eta_s = 100$ and $\eta_s = 200$ are again superimposed. Therefore, with $\eta_s = 20$, the shroud ROM does not allow to accurately capture the dynamical response of the shroud segment while $\eta_s = 100$ modes are sufficient. Concerning the blade displacement, see Fig. 19c, results are almost not affected by the value of η_s. Because computation times increase with the value of η_s as can be seen in Fig. 19d due to the increasing size of reduced matrices involved in the time integration scheme, the value $\eta_s = 100$ is retained in the following.

4.2.2 B-spline discretization

This section focuses on the results robustness in terms of the B-spline surface discretization. Indeed, the B-spline surface is built using a limited number of nodes on the upper surface of the shroud finite element model. The influence of the B-spline discretization has not been checked in previous work introducing the B-spline-based strategy for contact treatment [37]. However, the B-spline surface is key in the proposed strategy since (1) it is the mathematical tool used as contact interface to compute blade/shroud distances at each time step, (2) it is used to distribute the contact forces on the shroud boundary nodes, (3) the size of the shroud ROM depends on the number of nodes retained for the B-spline surface's construction, which directly affects the computation times. Therefore, a compromise between accuracy—with the B-spline surface's refinement—and computation times has to be found.

Different configurations are tested to analyze the effect of the number of nodes retained along x direction—M denotes the number of nodes in this direction—and along z direction—N defines the number of nodes in this direction—, see Fig. 20. The spline is progressively refined along x direction and then along z direction: $M = 5$ in Fig. 20a and $M = 11$ in Figs. 20b and 20c, while $N = 3$ in Fig. 20a and 20b, and $N = 7$ in Fig. 20c. The hatched areas highlight the blade/shroud contact location.

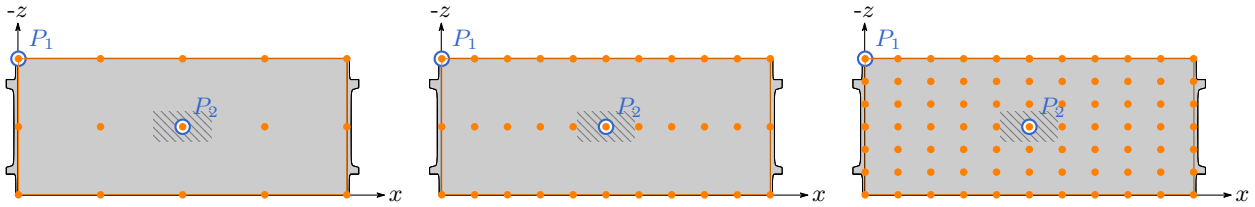

(a) 5×3 **(b)** 11×3 **(c)** 11×7

Figure 20. B-spline configurations with different discretizations.

Blade and shroud displacements obtained using the three boundary nodes configurations are shown in Fig. 21. In particular, the radial displacement of the shroud segment at point P_1 is given in Fig. 21a, and the radial displacement of the shroud segment at point P_2 in Fig. 21b. Radial displacement at the blade leading edge is depicted in Fig. 21c. The computation time of each simulation is reported in Fig. 21d. On the one hand, for both blade and shroud displacements (Figs. 21a, 21b and 21c), results differ from $M = 5$ (——) to $M = 11$ (——), meaning that retaining 5 nodes along x direction does not allow the spline surface to accurately follows the actual shroud surface. This can be explained by the curvature of the shroud surface along its circumferential direction. On the other hand, curves almost superimposed passing from $N = 3$ (——) to $N = 7$ (——). Because the shroud does not exhibits any curvature in the axial direction, results are not sensitive to the axial discretization.

The convergence of radial displacement at one node of the shroud segment has been shown for different time steps in Figs. 21a and 21b. In addition, the stress field within the full shroud finite element model at a given time $t = t^\star$ (identified in Figs. 21a and 21b) is shown in Fig. 22 for the three B-spline surface's discretizations, as well as a zoom on a limited area near sensor C. Time $t = t^\star$ is chosen because it corresponds to a time step of high amplitude

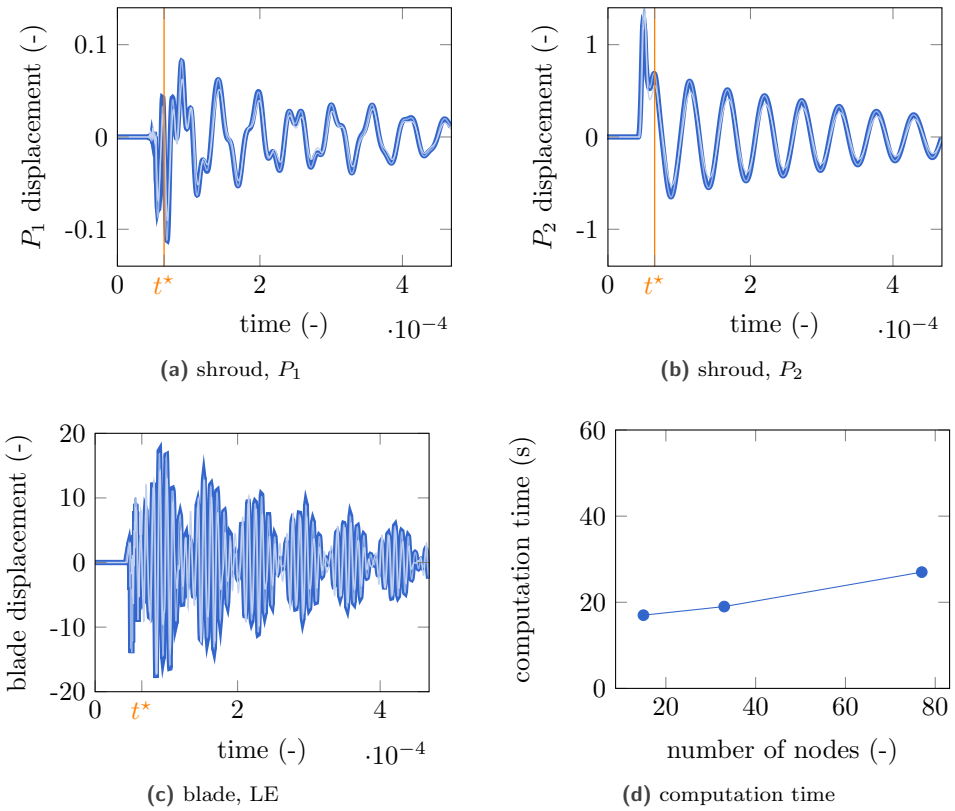

(a) shroud, P_1 **(b)** shroud, P_2

(c) blade, LE **(d)** computation time

Figure 21. Convergence with the spline discretization: 5×3 (——), 11×3 (——), 11×7 (——).

of vibration for the shroud, see Fig. 21b. The used color code, identical for the all subfigures, ranges from white—no constraints—to dark blue—high stress magnitude. The stress distribution within the structure is similar for the three spline discretizations. For each case, the highest stress levels are obtained in the vicinity of the four sensors because of the clamping boundary conditions.

Because this work focuses on the dynamical behaviour of the shroud segment, even if computation times increase with the number of retained nodes, as evidenced in Fig. 21d, the finest spline discretization with 11×7 nodes is considered in the following.

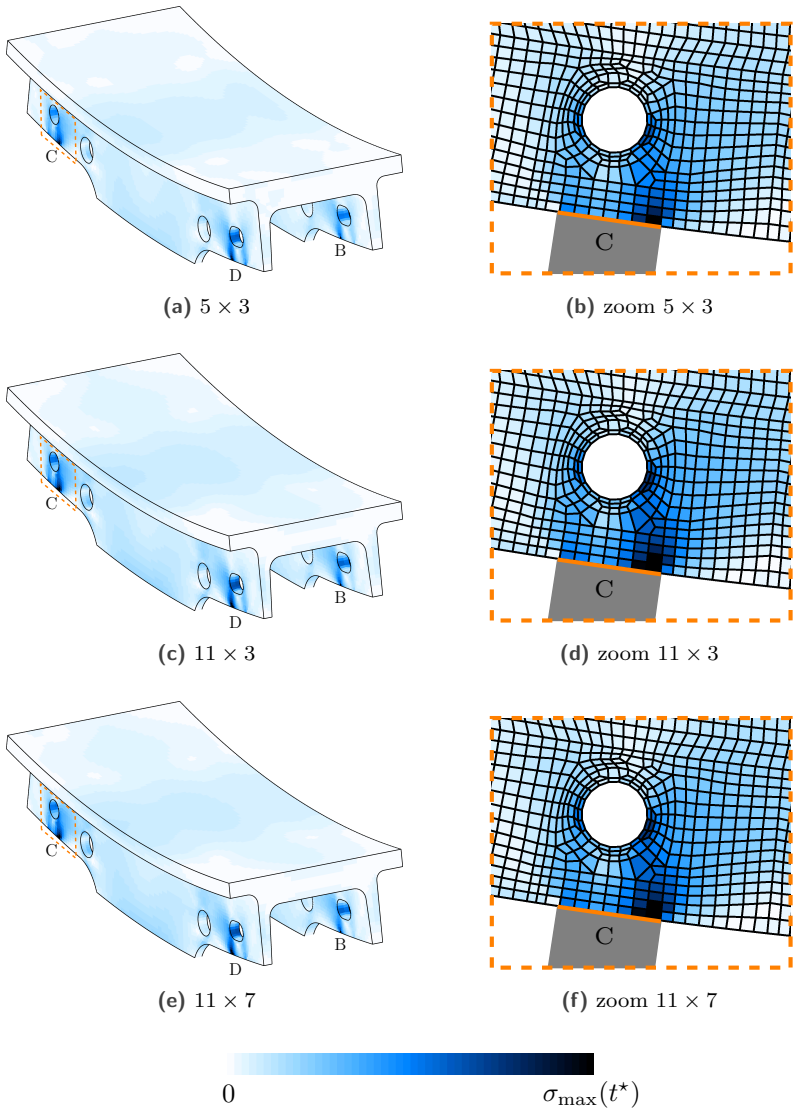

(a) 5×3 **(b)** zoom 5×3

(c) 11×3 **(d)** zoom 11×3

(e) 11×7 **(f)** zoom 11×7

(g) colour code

Figure 22. Stress field at $t = t^\star$ for different spline discretization.

4.2.3 B-spline size

Blade/shroud contact occurs over a limited area of the contact surface of the shroud segment. Therefore, the area on which the B-spline surface is constructed could be limited in the vicinity of the contact area. In this section, different sizes of the B-spline surface are analyzed. The tested configurations are illustrated in Fig. 23. The first configuration, see Fig. 23a, is built based on the same retained nodes than the one in Fig. 20c, except for the border nodes that have been removed from the selection. Then, configurations of Figs. 23b and 23c rely on retained nodes located near the center of the shroud upper surface. Two different discretizations along x direction are considered: $M = 3$ (see Fig. 23b) and $M = 9$ (see Fig. 23c). Because the discretization along z direction has a limited influence on the obtained results, see section 4.2.2, N is fixed to 3 for both configurations in Figs. 23b and 23c. Also, they are no common nodes between the ones retained in Figs. 23b and 23c and the boundary nodes selected in Fig. 23a.

Fig. 24 superimposes the results obtained with these three configurations, and with results obtained with the

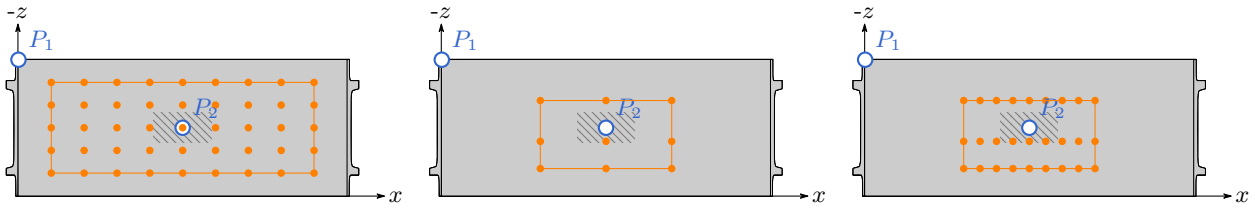

(a) 9×5 **(b)** 3×3 **(c)** 9×3

Figure 23. Tested B-spline configurations with different sizes.

finest B-spline surface in section 4.2.2 (11×7 configuration, see Fig. 20c). Radial displacements of the shroud segment at point P_1 and P_2 are shown respectively in Figs. 24a and 24b. Because the points P_1 and P_2 do not belong to the nodes retained in the ROMs' construction, a projection of the reduced shroud displacements in the finite element model is thus necessary to obtain the physical displacements drawn in Figs. 24a and 24b. The radial displacement at the blade leading edge is given in Fig. 24c. Computation times of each simulation are reported in Fig. 24d. For both blade and shroud displacements, minor discrepancies between curves can be observed, especially for the 3×3 configuration (——). This validates the robustness of the obtained results with the B-spline surface's size. Also, results are not dependent of the choice of boundary nodes. They can be changed without affecting the results. Computation times again increases with the number of retained nodes, see Fig. 24d.

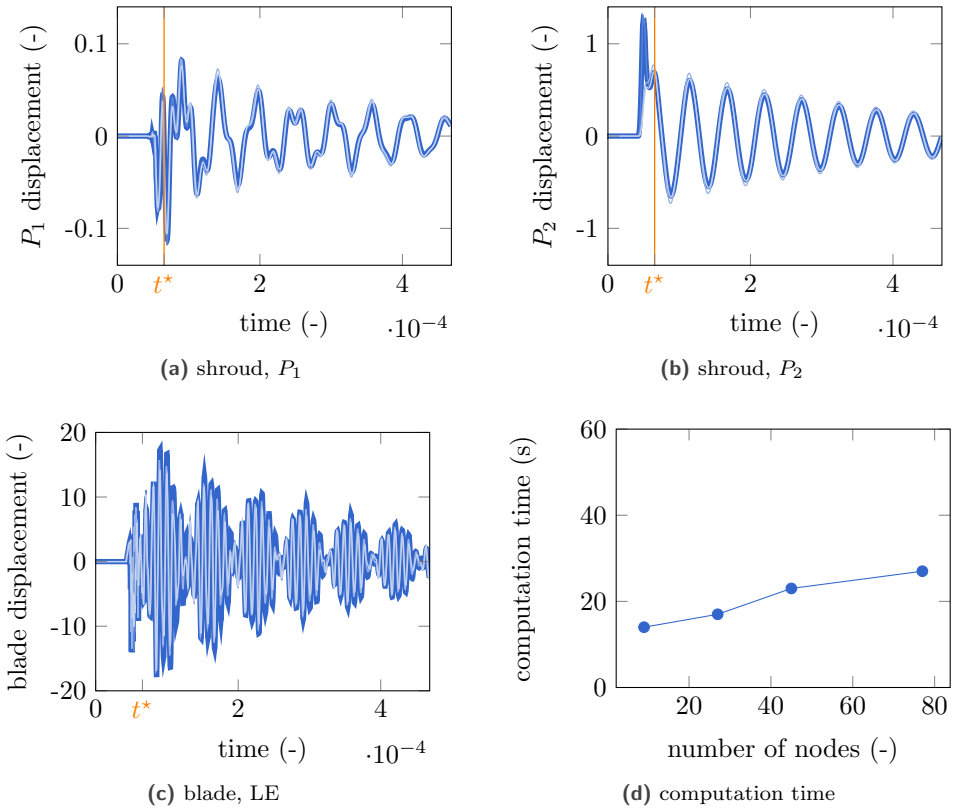

(a) shroud, P_1 **(b)** shroud, P_2

(c) blade, LE **(d)** computation time

Figure 24. Convergence with the B-spline sizes: 11×7 (——), 9×5 (——), 3×3 (——) and 9×3 (——).

Stress fields within the full shroud finite element model at the given time $t = t^\star$ for each B-spline configuration

are depicted in Fig. 25. A zoom in the vicinity of sensor C, where high stress variations are evidenced, are also given. A similar stress distribution is obtained for each tested configuration, with the highest stress variations in the vicinity of the clamping areas. The stress distribution is also similar with the one in Fig. 22, for the previously tested configurations.

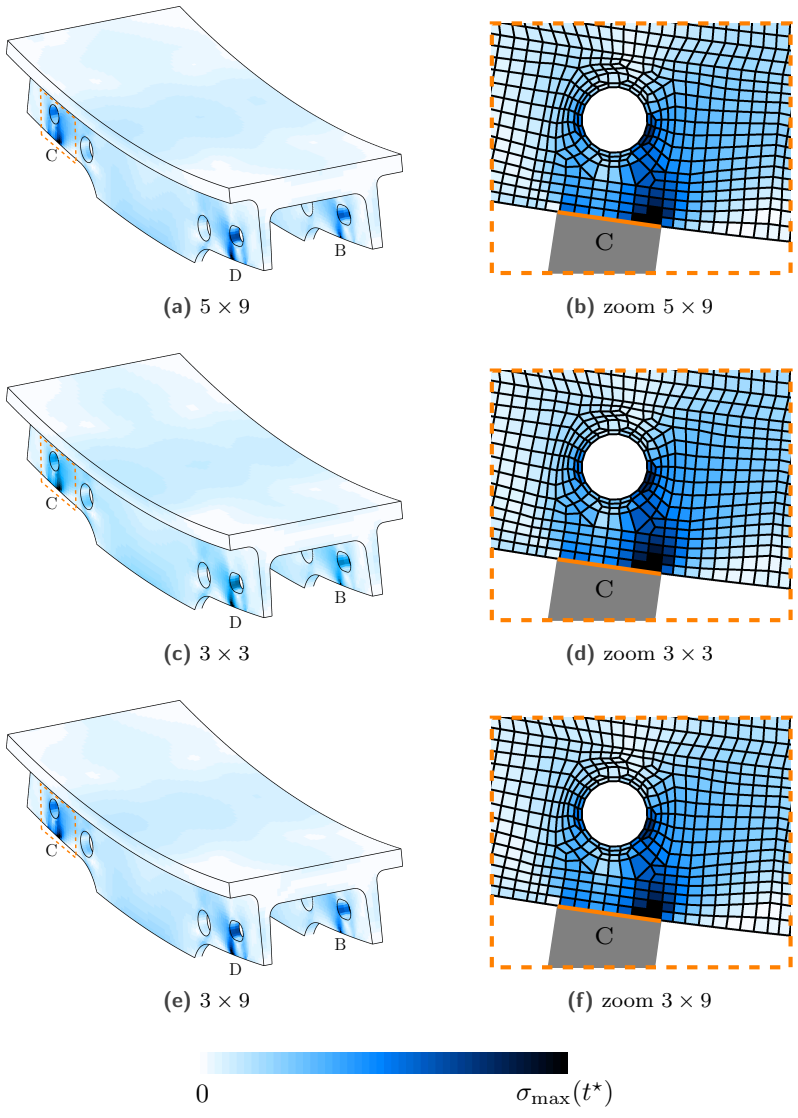

(a) 5×9 **(b)** zoom 5×9

(c) 3×3 **(d)** zoom 3×3

(e) 3×9 **(f)** zoom 3×9

(g) colour code

Figure 25. Stress field $t = t^\star$ for different B-spline sizes.

The analysis of the robustness of the results with the B-spline size and the nodes selection allow to ensure the independence of the results with modes retained in the shroud ROM. In the following, the finest configuration, with 11×7 boundary nodes, is retained because the shroud segment is the focus of this work.

4.2.4 Abradable layer's discretization

The convergence of the blade and shroud displacements with the number of elements in the abradable layer's mesh is verified in this section. The discretization of the abradable layer's mesh influences the prediction of the

wear profile, but also on the contact forces distribution. Simulations with different number of elements along the shroud circumferential direction—denoted N_{ab}, see Fig. 15—are considered, ranging from 5,000 to 100,000. Results obtained for each N_{ab} value are superimposed in Fig. 26. In particular, the radial displacement at points P_1 and P_2 on the shroud segment are given in Figs. 26a and 26b respectively, and the radial displacement at the blade leading edge is shown in Fig. 26c. Blade displacements (Fig. 26c) are more affected by the abradable layer's mesh discretization than the shroud displacements (in Figs. 26a and 26b). Convergence of both blade and shroud displacements is achieved for $N_{ab} \geq 10,000$. The computation times corresponding to each N_{ab} value are given in Fig. 26d. They are practically unaffected by the number of abradable elements. In the following, 10,000 elements are used.

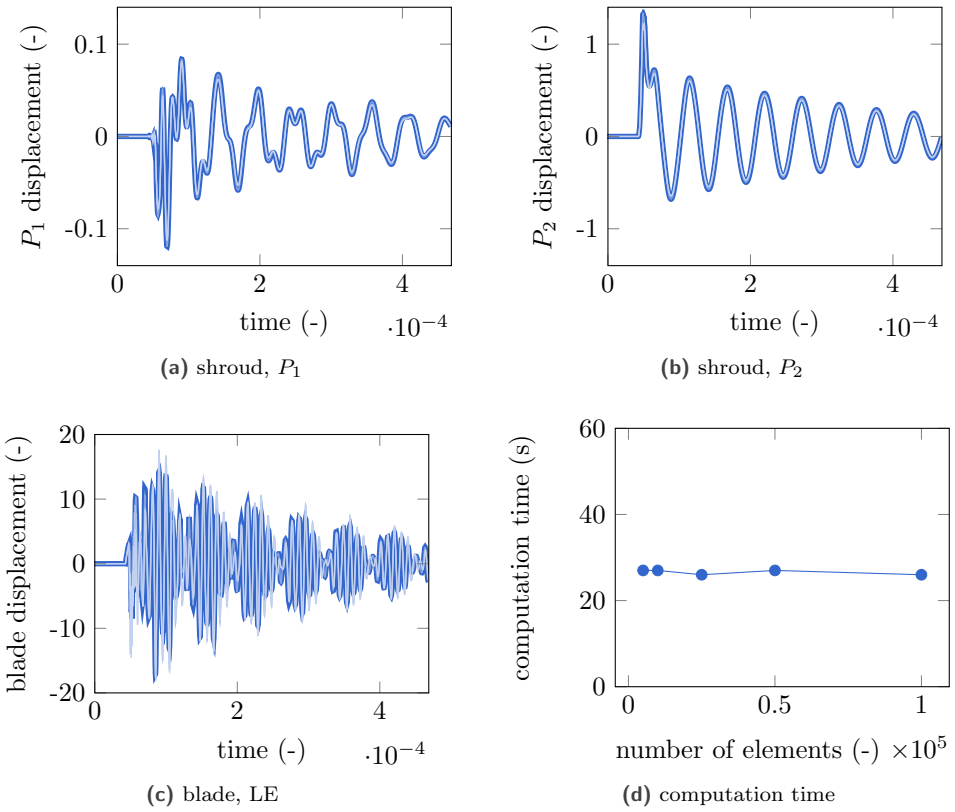

(a) shroud, P_1 **(b)** shroud, P_2

(c) blade, LE **(d)** computation time

Figure 26. Convergence with the abradable layer's discretisation: $N_{ab} = 5,000$ (——), $N_{ab} = 10,000$ (——), $N_{ab} = 25,000$ (——), $N_{ab} = 50,000$ (——), $N_{ab} = 100,000$ (——).

5 Numerical simulation of the experimental set-up

5.1 Parameters calibration

The calibration of the abradable layer's plastic modulus, denoted K_{ab}, is carried out on the test case c_1. Simulations are performed on the 25 first percents of the total test time to prevent from blade wear, see section 2.5.3, which corresponds to several hundreds of blade revolutions.

The mechanical properties of the shroud segment, as well as the abradable layer's Young's Modulus E_{ab}, have been identified through dedicated material testings, not detailed here for the sake of brevity. These variables are thus fixed in the numerical model. However, the plastic modulus K_{ab} of the abradable layer has to be calibated. In the theoretical definition of the elasto-plastic law used to model the abradable layer [30], the plastic modulus influences

the contact force magnitude. Therefore, this variable is key to calibrate the numerical model with experimental forces. Because the modeling of the abradable layer using 1D-rod elements is a simplified macroscopic view of the wear mechanism to be able to update at each time step the abradable layer's profile, the value of K_{ab} in the numerical model can highly differ from its actual physical value. It acts as a purely numerical parameter in the time integration algorithm.

Figure 27 shows the upper envelope of the time evolution of the forces obtained numerically with different K_{ab} values: $K_{\text{ab}} = \frac{E_{\text{ab}}}{300}$, $K_{\text{ab}} = \frac{E_{\text{ab}}}{400}$, $K_{\text{ab}} = \frac{E_{\text{ab}}}{600}$ and $K_{\text{ab}} = \frac{E_{\text{ab}}}{800}$. Experimental data are added in gray. All data are normalized for the sake of confidentiality. As can be seen in Fig. 27, the higher K_{ab} value, the higher the resulting forces. The K_{ab} value that suits the best with the experimental data is $K_{\text{ab}} = \frac{E_{\text{ab}}}{400}$ (——). This value of K_{ab}, calibrated on test case c_1 only, is fixed in the following for all tested configurations.

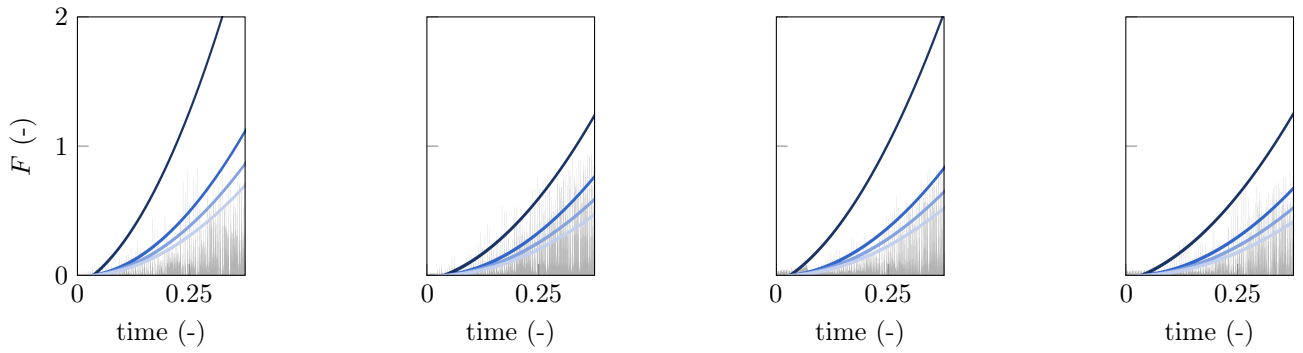

(a) A **(b)** B **(c)** C **(d)** D

Figure 27. Experimental and numerical forces at each sensor for test case c_1, with different K_{ab} values: $\frac{E_{\text{ab}}}{300}$ (——), $\frac{E_{\text{ab}}}{400}$ (——), $\frac{E_{\text{ab}}}{600}$ (——), $\frac{E_{\text{ab}}}{800}$ (——).

Modal damping values of the two first modes of the shroud segment are fixed in the numerical model: they are set to the experimental values. But the modal damping of higher frequency modes are unknown and are used to calibrate the numerical model. A zoom on the experimental signal of test case c_1 for 6 successive contacts is shown in Fig. 28a. It can be seen that, between two successive contact events, the signal is damped. Fig. 28b superimposed

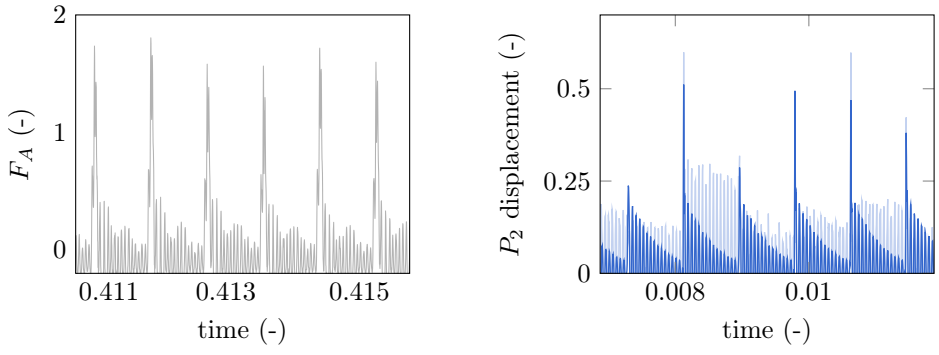

(a) experimental **(b)** numerical

Figure 28. Modal damping calibration.

the numerical displacement of the shroud segment at node P_2 in the radial direction with (1) a modal damping identical for higher frequency modes—equal to the damping value of the first mode— (——), and the numerical

displacement after modal damping calibration (——). Before calibration, the signal exhibits a low damping between two successive contacts: the modal damping of higher modes has to be increased. The calibrated value allow to follow the experimentally observed behaviour.

The wear profile obtained using the calibrated model at the end of the simulation of test case c_1 is shown in Fig. 29. The abradable layer covers all the shroud segment, from angular position -α_s to α_s. The coating is worn in a limited area, at the impact location. The shape of the wear is an arc circle because of the circular trajectory of the blade. The wear depth corresponds to the targeted value—25% of the experimental value—, which is evidenced with a blue horizontal dotted line.

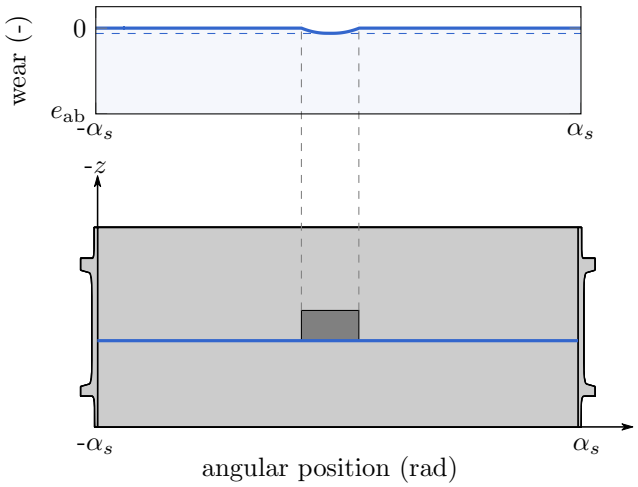

Figure 29. Wear profile (——), targetted value (- - -).

5.2 Simulation of the other test cases

Numerical parameters obtained from the model calibration on configuration c_1 only are used now to simulate test cases c_2, c_3, c_4 and c_5. The force at A, B, C and D locations are compared with the corresponding experimental data for each test case in Fig. 30. Numerical results (in blue) and experimental signals (in gray) are superimposed over the first 25 percents of the total tests duration.

A good agreement of the numerical results—obtained using parameters calibrated on test case c_1 only—with the experimental data is observed. For each simulated test case, the same order of magnitude of forces at each sensor than the experiments is obtained. The time evolution of sensor forces follows the same trend, before the change of slope due to non-modelized blade wear. For test case c_2, large differences between the time evolution of experimental and numerical sensor forces are observed: this is due to a sudden slope change in the experimental signals that appears before $t_{25\%}$. Forces are therefore over-estimated numerically for this case since no blade wear is modeled. The relative difference of the maximum force for each test case is also given in Fig. 30. The largest difference is obtained for test case c_2 due to its sudden slope change.

An important achievement of this study is to predict the maximum force submitted by the shroud segment following contact events. Therefore, the maximum force during the simulated duration ($t \in [0, t_{25\%}]$) are synthesized for each sensor in Fig. 31. The same order of magnitude and the same trend of force distribution between the four sensors is obtained for each test case. Considering the disparities and noise in the experimental data, some deviations in the maximum force values is unavoidable. But the numerical force distribution remains coherent with experiments for each test case, meaning that the model updating is relevant for the different impact locations. Therefore, the numerical model is assumed reliable and validated.

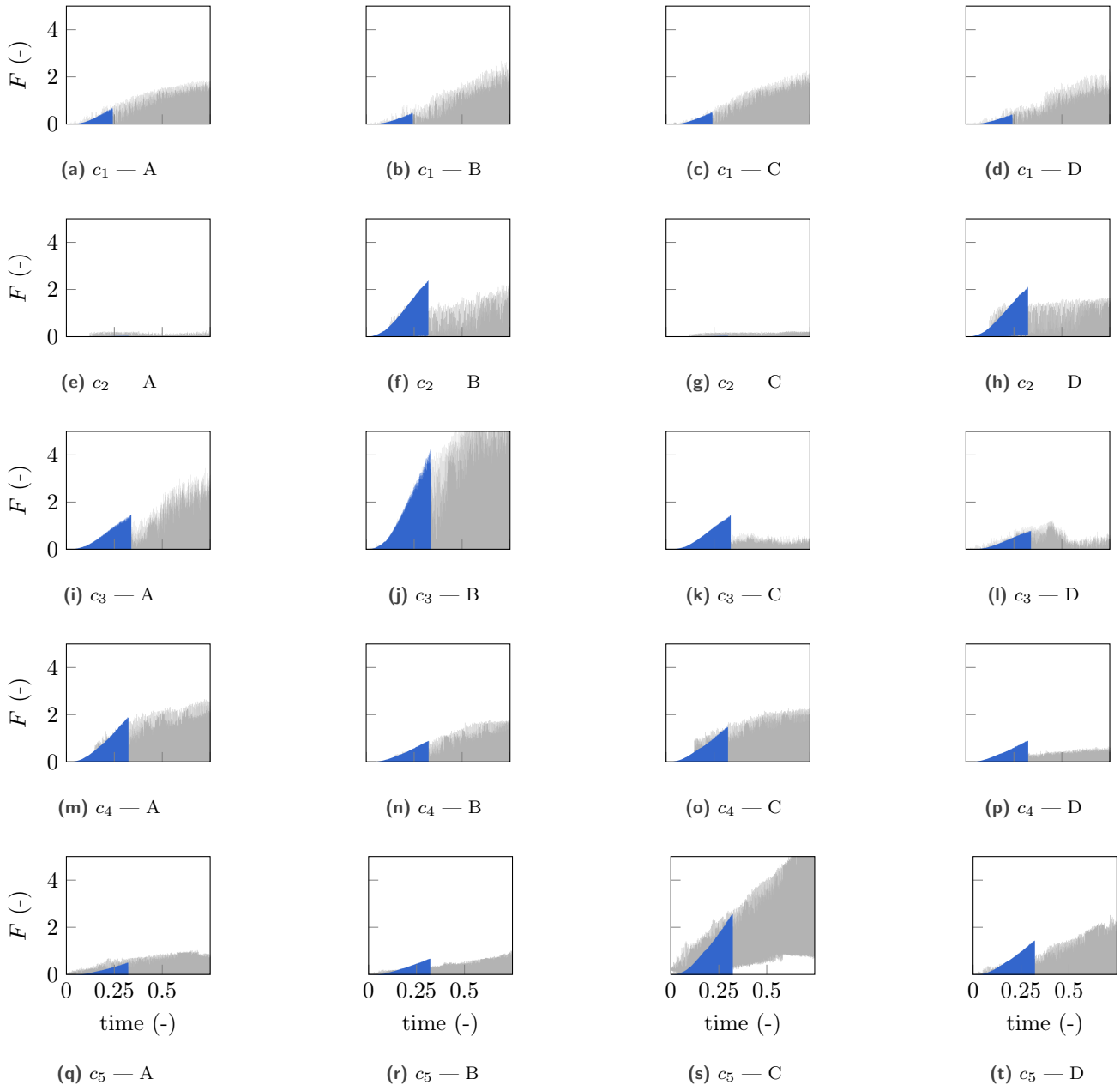

(a) c_1 — A **(b)** c_1 — B **(c)** c_1 — C **(d)** c_1 — D

(e) c_2 — A **(f)** c_2 — B **(g)** c_2 — C **(h)** c_2 — D

(i) c_3 — A **(j)** c_3 — B **(k)** c_3 — C **(l)** c_3 — D

(m) c_4 — A **(n)** c_4 — B **(o)** c_4 — C **(p)** c_4 — D

(q) c_5 — A **(r)** c_5 — B **(s)** c_5 — C **(t)** c_5 — D

Figure 30. Comparison of experimental (■) and numerical (■) sensor forces for each test case using parameters calibrated on test case c_1 only.

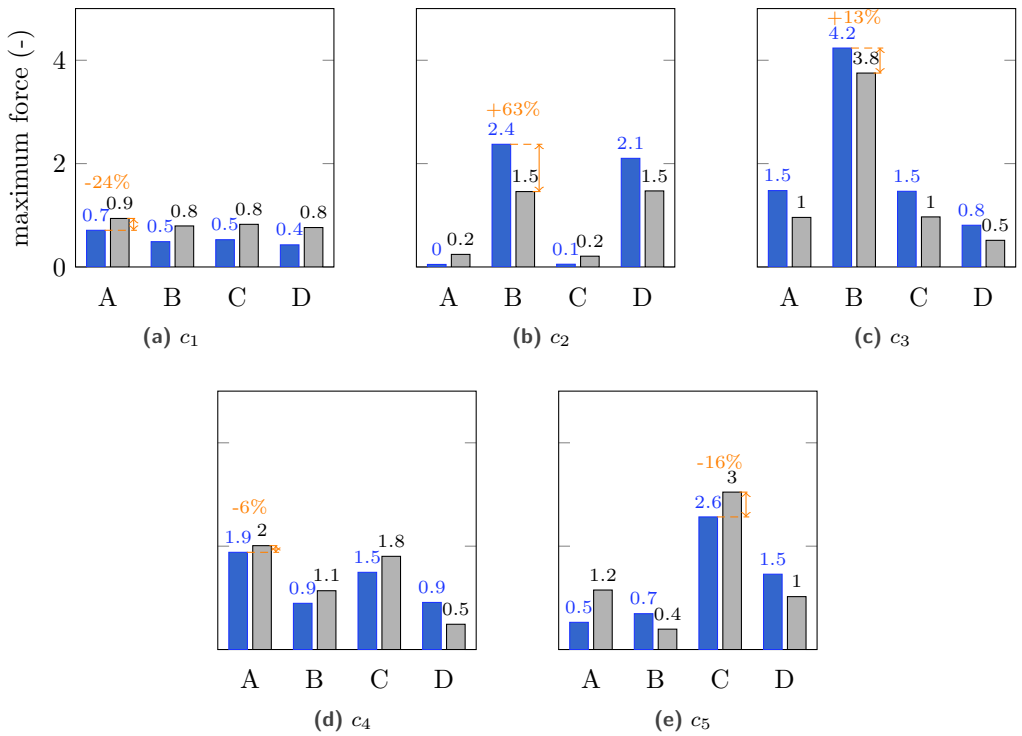

Figure 31. Comparison of experimental (■) and numerical (■) sensor forces for each test case.

6 Numerical simulations of engine-like conditions

6.1 Parameters of interest

The confrontation between experimental observations and numerical results underlined the relevance of the employed numerical strategy. This same numerical model is now used to simulate impact loadings in engine-like conditions, using the numerical model of the actual turbine blade. The influence of the following parameters on the resulting forces on the shroud segment is analyzed in this section:

radial velocity: The radial blade/shroud relative velocity v_p in operating conditions slightly differ from the one applied on the experimental test bench. It is set here to the most probable speed range that can occur after a full throttle: $v_p \in \left[v_p^{min} - v_p^{max}\right]$.

contact location: In the actual engine configuration, blade/shroud contacts occur at the blade mid-chord (MC). However, for a variety of reasons (such as shroud segment tip over, thermal expansion or significant wear...) contact may be initiated at the blade leading edge (LE) or trailing edge (TE). The location of the LE, MC and TE of the engine blade on the shroud segment can be seen in Fig. 32. Red dots correspond to the projection of the nodes retained in the engine blade's ROM on the shroud segment. For comparison, the projection of retained nodes of the mock blade's ROM on the shroud segment appears in dark gray: the chord of actual turbine blade exhibits a much more significant curvature and width compared to the mock blade.

number of blades: The choice of the number of blades in contact with the shroud segment per rotor revolution will affect the system dynamics and the resulting forces on the shroud segment. Unavoidable manufacturing imperfections yield a certain variability of each blade length. It is thus assumed that contact is initiated between the shroud segment and the longest blade. After a certain time however, once the longest blade has been worn off following contacts, comes a time where all blades may impact the shroud segment. It thus seems relevant to also consider a scenario for which each of the 60 blades impacts the shroud segment.

angular speed: The nominal engine angular speed, at which simulations are carried out, is denoted Ω. The effect

of an angular speed deviation of −10% and +10% is also analyzed. The particular case of 0.65Ω is also investigated because it corresponds to a resonance speed.

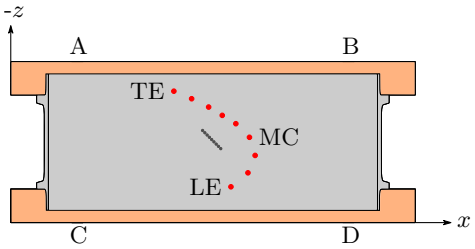

Figure 32. Location of the retained nodes for the ROM of the engine blade (●) and the mock blade (•).

6.2 Radial velocity

The influence of the relative shroud/blade radial velocity v_p is analyzed in this section. Contacts occur at the blade mid-chord, the nominal angular speed Ω is used, and simulations are carried out with one blade in contact per rotor revolution. The used parameters are summarized in Table 1.

v_p	impact	angular speed	blade number
$\left[\mathbf{v_p^{min}} - \mathbf{v_p^{max}}\right]$	MC	Ω	1

Table 1. Numerical parameters for the influence of the radial velocity.

Figure 33a shows the radial displacement at the center of the shroud segment, *i.e.* at point P_2, for different radial velocities v_p: $v_p = v_p^{\min}$, $v_p = 0.5\left(v_p^{\min} + v_p^{\max}\right)$ and $v_p = v_p^{\max}$. The maximum force level at the four sensors (A, B, C and D) achieved for each simulation is reported in Fig. 33b. The final wear depth is identical for all simulations. Logically, the duration of the simulation is shorter for higher v_p values. As the velocity v_p increases, the amount of removed wear per blade contact grows. The induced shroud vibrations increase, which lead to a higher slope in the time evolution of the shroud displacement. At the end of the simulations, when the targeted wear depth is achieved, the shroud vibration amplitude is slightly higher for increased v_p values. The higher the amplitude of vibration, the higher the forces at the four sensors. This leads to an increasing force level with v_p, as can be seen in Fig. 33b. In

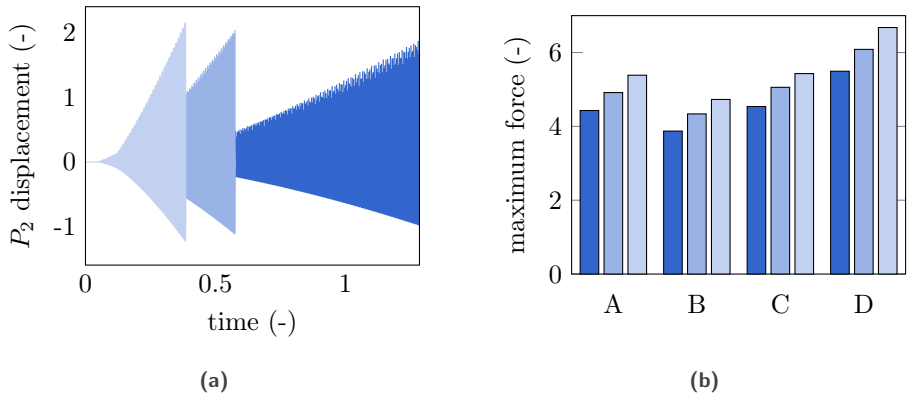

(a) **(b)**

Figure 33. Shroud segment's displacement at point P_2 (a) and maximum sensor forces (b) for $v_p = v_p^{\min}$ (■), $v_p = 0.5\left(v_p^{\min} + v_p^{\max}\right)$ (■), $v_p = v_p^{\max}$ (■).

the following, only the highest value of v_p is retained in order to obtain a conservative estimate of contact forces during an interaction.

6.3 Contact location

This section focuses on the influence of the contact location along the blade chord on the contact forces estimated at the back of the shroud segment. In the nominal configuration, contacts occur at the blade mid-chord. The numerical model advantageously allows to simulate interactions featuring contacts located only at the blade leading or trailing edges. The blade rotates at its nominal angular speed Ω, and simulations are carried with one blade. The different simulation parameters are summarized in Table 2.

v_p	impact	angular speed	blade number
$v_p^{\max}$	**LE, MC, TE**	Ω	1

Table 2. Numerical parameters for the influence of the impact location.

The maximum radial displacement of the blade is depicted in Fig. 34a for a contact occurring at the blade's LE, MC and TE. For each case, the node of maximum displacement corresponds the one on which contact occurs. The

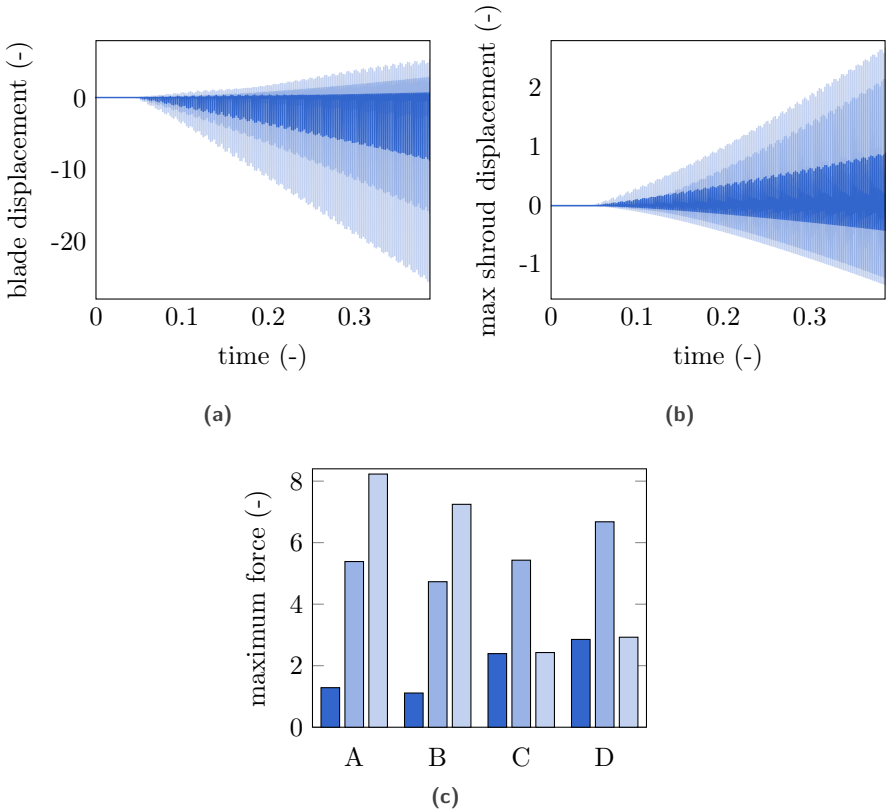

Figure 34. Blade displacement (a), maximum shroud segment's displacement (b) and maximum sensor forces (c) for contacts at LE (■), MC (■), TE (■).

amplitude of vibration is larger for a contact at the trailing edge (■) rather than a contact at mid-chord (■). An impact at the leading edge (■) exhibits the lowest vibration amplitudes. This observation can be directly related to the blade stiffness: applying the same force magnitude at trailing edge, mid-chord or leading edge leads to decreasing blade deformation. The higher the blade vibration amplitude, the higher the induced shroud displacement. This is confirmed by the radial displacement at point P_2 of the shroud segment plotted in Fig. 34b. The resulting forces at each sensor are given in Fig. 34c. For a contact at the leading edge, because of the smaller vibration amplitude of

the shroud segment, the resulting force levels are lower. Nevertheless, the leading edge location is close to sensors C and D (see Fig. 32), higher force values are obtained for these two sensors than for sensors A and B. Then, for a contact at mid-chord—*i.e.* a contact occurring in the vicinity of the center of the shroud segment—, forces are spread more uniformly between the four sensors. Finally, for an impact localized at the trailing edge, higher force amplitudes are obtained due to the higher shroud displacements. Since the trailing edge is closer to sensors A and B, the latter exhibit higher force values than sensors C and D.

Therefore, the most detrimental configuration is found to be a contact occuring at the blade trailing edge.

6.4 Blade number

Two contact scenarios are investigated: (1) simulations with one blade in contact per revolution, and (2) simulations for which the contact may occur on the 60 blades of the rotating bladed disk. All blades are clamped at their roots, meaning that the disk displacement is neglected. For these two scenarios, simulations with a contact at LE, MC and TE are carried out. The angular speed is assumed constant over the simulations and equal to the nominal angular speed Ω. The simulation parameters are recalled in Table 3.

v_p	impact	angular speed	blade number
$v_p^{\max}$	**LE, MC, TE**	Ω	**1, 60**

Table 3. Numerical parameters for the influence of the blade number.

The forces obtained at each sensor for simulations with one and 60 blades are shown in Figs. 35a, 35b and 35c with contact at the LE, MC and TE respectively. The first observation is that, for the three cases, the obtained forces are lower for the simulations with 60 blades than with one blade in contact. This can be explained by the fact that, when 60 blades are considered in the numerical model, each blade removes 60 times less abradable coating's depth. A second observation is that, while for simulations with a single blade the force distribution depends on the contact location, forces remain rather uniformly distributed between the four sensors for simulations with 60 blades.

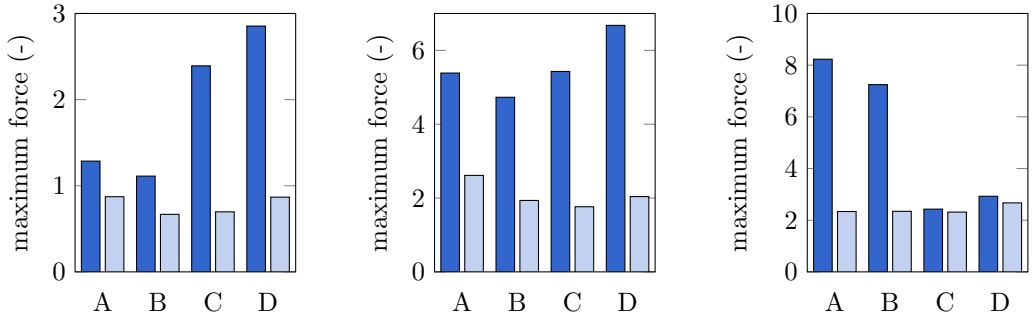

(a) LE **(b)** MC **(c)** TE

Figure 35. Maximum sensor forces for contacts at LE (a), MC (b) and TE (c): simulations with one blade (■), 60 blades (■).

To explain this second observation, the contribution of the 50 first modes in the shroud segment's dynamical response over one rotor revolution is depicted in Fig. 36 for simulations with one blade, and in Fig. 37 for simulations with 60 blades. Denoting T the time of one rotor revolution, contact occurs every T s for simulations with one blade, and every $\frac{T}{60}$ s for simulations with 60 blades. Comparing the mode participation at LE, MC and TE for both scenarios, two main differences can be evidenced. On the one hand, higher frequency modes are involved in the shroud segment's response for simulations with 60 blades. On the other hand, the structure vibrates along its first vibration mode between two contact events for cases with one blade. However, the participation of the first mode disappears for simulations with 60 blades. Indeed, repeated contacts do not allow the shroud segment to vibrate along its first vibration mode before the next contact. This difference in the dynamical behaviour explains the change in force distribution between the four sensors.

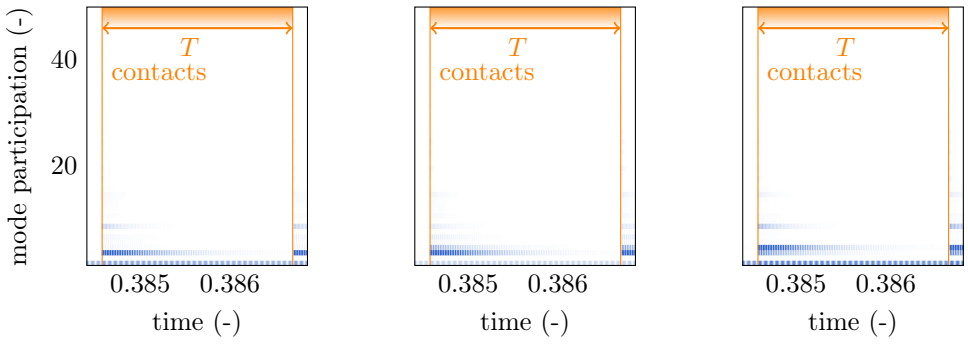

(a) LE **(b)** MC **(c)** TE

Figure 36. Mode participation to the shroud response for simulations with one blade.

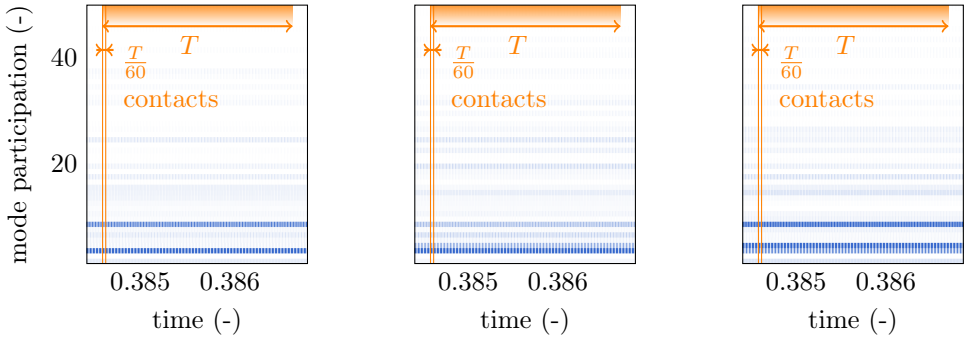

(a) LE **(b)** MC **(c)** TE

Figure 37. Mode participation to the shroud response for simulations with 60 blades.

Figure 38a shows the radial displacement at point P_2 for simulations with one blade impacting the shroud segment at MC. Shroud displacement varies between positive and negative values in time. As evidence in the zoom of Fig. 38b, shroud vibrations are damped between two contact events. A further zoom, shown in Fig. 38c, evidences that between a contact moment and $\frac{T}{60}$ s later, the shroud displacement still has a positive value. This explains the shroud behaviour observed for simulations with 60 blades. Indeed, for the 60 blades scenario, the radial displacement of the shroud segment at point P_2 remains positive, as can be seen in Fig. 39a. Figure 39b is a zoom on several contacts at the end of the simulation. The orange vertical lines evidence contact occurrences. Between two successive contacts, the structure does not have enough time to come back to negative displacement values. Therefore, the comparison of the shroud segment's displacement for simulations with one and 60 blades also evidences the difference in its dynamics with the number of impacts per rotor revolution.

The configuration with one blade in contact per rotor revolution is more detrimental for the shroud segment's integrity because of the higher force magnitudes and the loading dissymmetry between the four sensors.

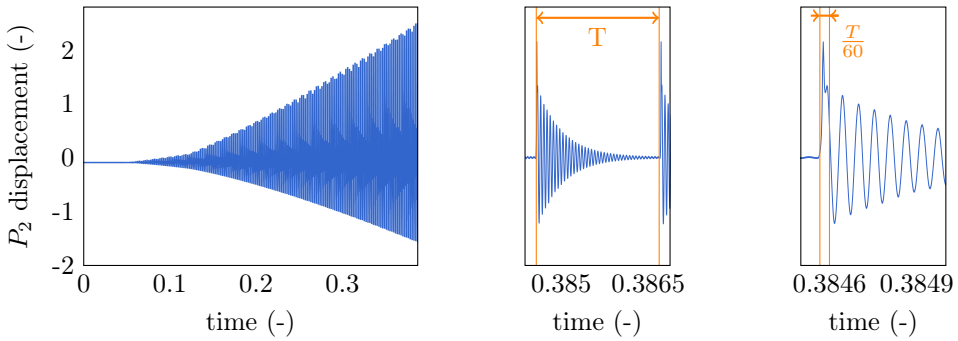

(a) **(b)** zoom **(c)** zoom

Figure 38. Shroud radial displacement (a) and zooms (b and c) for simulations with one blade and contact at MC.

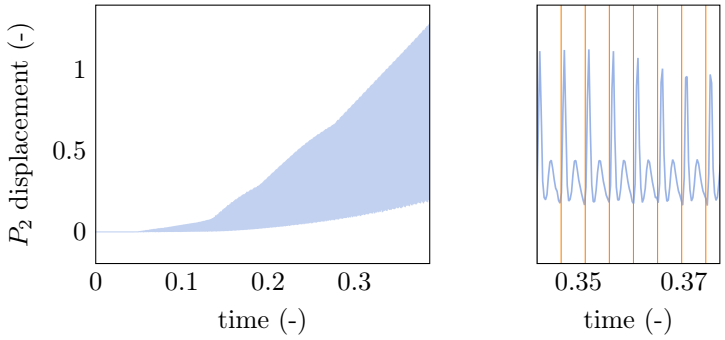

(a) **(b)** zoom

Figure 39. Shroud radial displacement (a) and zoom (b) for simulations with 60 blades and contact at MC.

6.5 Angular speed

The last parameter of interest is the rotor angular speed. The angular speed is varied from −10% and +10% of the nominal value. The particular angular speed 0.65Ω is also analyzed. An impact at blade mid-chord is considered and simulations are carried out with one and 60 blades, as summarized in Table 4.

v_p	impact	angular speed	blade number
$v_p^{\max}$	MC	**0.65Ω, 0.9Ω, Ω, 1.1Ω**	**1, 60**

Table 4. Numerical parameters for the influence of the angular speed.

The radial displacement of the shroud segment at point P_2 is depicted in Fig. 40a for simulations with one blade. Results obtained for 0.9Ω, Ω and 1.1Ω are superimposed. Since the blade/shroud relative velocity v_p is identical for each case, the targeted wear depth is achieved after the same time and the simulation durations are the same for the three angular speeds. When the rotor angular speed increases, the amount of wear per revolution decreases. Consequently, displacement amplitudes also decrease, see Fig. 40a, and the resulting forces at each sensor are reduced as evidenced in Fig. 40b.

The radial displacement of the shroud segment at node P_2, obtained for simulations with 60 blades, is depicted in Fig. 41a for angular speeds equal to 0.9Ω, Ω and 1.1Ω. A zoom on several contacts—vertical orange lines highlight contact occurrences—at the end of the simulations is given in Fig. 41b, 41c and 41d for the angular speeds 0.9Ω,

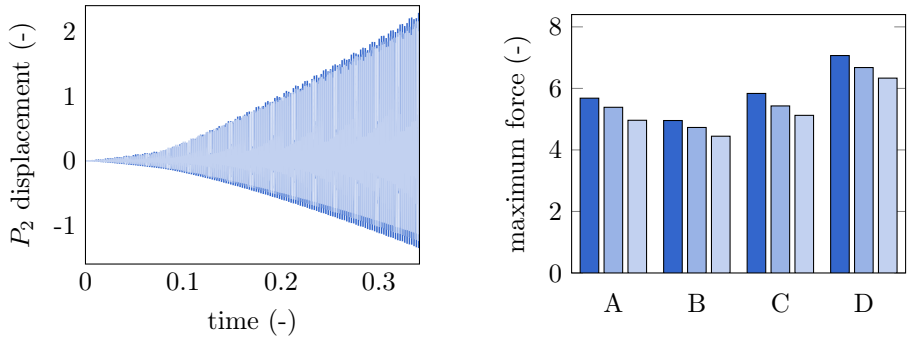

(a) (b)

Figure 40. Shroud displacement (a) and maximum force at each sensor (b) for angular speed 0.9Ω (■), Ω (■) and 1.1Ω (■) for simulations with one blade.

Ω and 1.1Ω respectively. As for simulations with one blade in contact, the radial velocity v_p and the targetted wear depth are identical for the three cases, which leads to the same simulated duration. However, in this case, because increasing the angular speed results in shorter time between two successive contacts, the shroud segment's displacement has a higher (positive) value when the next contact occurs. Therefore, displacement amplitude increases with the angular speed.

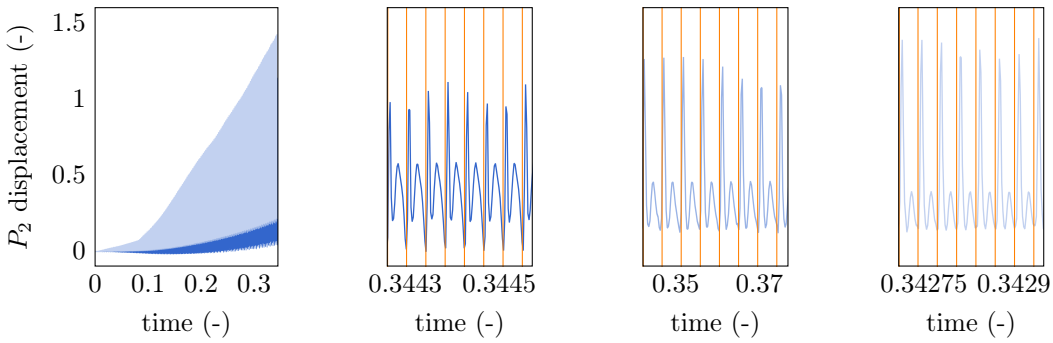

(a) (b) 0.9Ω (c) Ω (d) 1.1Ω

Figure 41. Shroud displacement (a) and zoom (b,c,d) for angular speed 0.9Ω (■), Ω (■) and 1.1Ω (■), for simulations with 60 blades.

Fig. 42a shows the radial displacement of the shroud segment at point P_2 for simulation carried out at a rotor angular speed equal to 0.65Ω (■) and Ω (■). A zoom on several contacts at the end of the simulation at 0.65Ω is given in Fig. 42b. As evidenced with the vertical orange lines in Fig. 42b marking contact events, the particular angular speed 0.65Ω corresponds to contacts synchronized with the time at which the shroud segment reaches its minimum displacement value. The amplitude of vibration achieved at this specific angular speed are more than seven times higher than with the nominal value, see Fig. 42a. The resulting maximum sensor force reaches 6.5 times the values obtained at Ω, as shown in Fig. 42c. This clearly highlights the criticality of this particular configuration, which may lead to shroud damage in operation. Should such behaviour occur for an angular speed within the nominal operating range, design updates may be required in order to avoid potential damages.

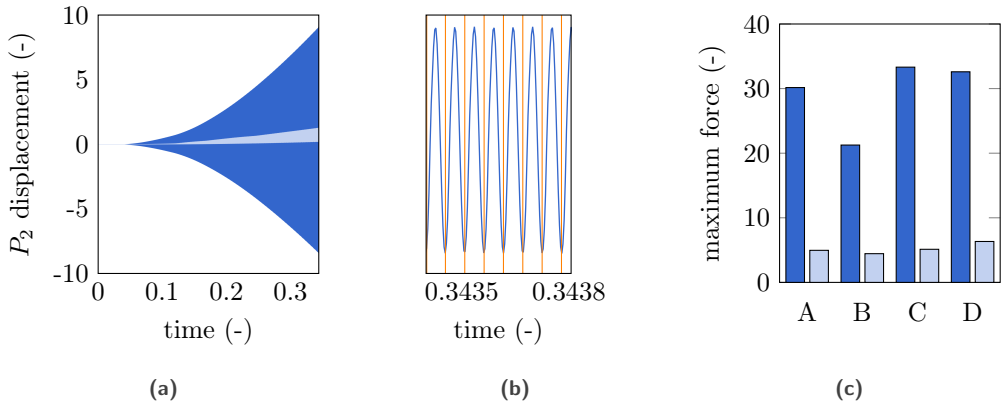

Figure 42. Shroud displacement (a), zoom (b), and maximum sensor forces (c) for simulations with 60 blades at 0.65Ω (■) and Ω (■).

6.6 Partial conclusion

From an industrial prospective, it is critical to estimate stresses resulting from impact loadings on the shroud segment following contacts with the rotating blades. Indeed, CMC materials feature much lower admissible stresses than titanium alloys. The use of CMC materials for these components thus called for a detailed analysis of stress levels in order to ensure engine safety. The numerical model allows to investigate impact loadings in different configurations (radial velocity, contact location, blades number, angular speed) to simulate engine-like conditions. For the sake of confidentiality, stresses within the shroud segment are not provided. However, for the studied configurations, the conservative numerical estimation of stress levels within the shroud segment following contacts provides values significantly lower than maximal admissible stresses. These results support the viability of the use of CMC materials in turbine shrouds.

7 Conclusion

This work proposes an experimental and numerical estimation of forces within a shroud segment made of ceramic matrix composite (CMC) material following contact events.

The experimental test bench consists in three mock blades notched in a simplified rotor, that impact the CMC shroud segment. An abradable layer is deposited onto the shroud segment's contact surface. Four sensors located under the shroud segment give access to the forces during the tests. Different contact scenarios featuring various impact locations on the shroud segment are investigated. A significant level of wear on the blade is evidenced at the end of each test. This wear is associated to complex thermo-mechanical phenomena as high temperatures along the blade/shroud segment interface are observed.

A numerical strategy, relying on an in-house tool dedicated to the simulation of contact interactions, is proposed to predict numerically the experimentally observed interactions. As a first approach, the focus is narrowed to the first 25 percents of each test, a period of time over which thermo-mechanical effects are assumed negligible. Simulations are based on reduced order models featuring nonlinear contact interfaces. A B-spline surface is used along the contact interface as a smoothening procedure for the definition of the contact surface normal vector. An extensive validation of the proposed numerical strategy is carried out. Convergence of blade and shroud segment's displacements with respect to key numerical parameters—such as the time step of the time integration scheme, and the contact surface's discretization—is carefully assessed.

The calibration of the numerical model is performed considering a single test configuration. This calibrated model is then employed for the simulation of the other test cases. Numerical predictions of the forces at the four sensors location are in good agreement with forces acquired experimentally. Particular attention is paid to the ability of the numerical model to accurately predict the distribution of forces between the four sensors.

The calibrated numerical model is then employed for the simulation of blade/shroud segment interactions considering engine-like conditions which could not be reproduced experimentally. The influence of several parameters—radial velocity, impact location, number of blades in contact and angular speed—underlines the sophisticated dynamics of the shroud segment, particularly in the case of interaction considering the full 60-blade bladed disk. In the end, the successful calibration of the proposed numerical strategy brings forward the possibility to enhance the shroud segment design in order to be more robust with respect to unavoidable contact events.

Acknowledgment

This research was supported by Safran Aircraft Engines. The authors are grateful to Antoine Millecamps, former engineer of Safran Aircraft Engineers who initiated and contributed to this research work throughout the years on both experimental and numerical aspects.

References

[1] Marsh, G., 2012. "Aero engines lose weight thanks to composites". *Reinforced Plastics,* ***56***(6), pp. 32–35. doi: 10.1016/S0034-3617(12)70146-7.

[2] Chen, N., Zhang, H., Ning, F., Xu, Y., and Huang, W., 2006. "An effective turbine blade parameterization and aerodynamic optimization procedure using an improved response surface method". In Proceedings of the ASME Turbo Expo 2006. doi: 10.1115/GT2006-90104.

[3] Lee, K.-S., Kim, K.-Y., and Samad, A., 2008. "Design optimization of a low-speed fan blade with three-dimensional RANS analysis". *Journal of Mechanical Science and Technology,* ***22***(10). doi: 10.1007/s12206-008-0724-y.

[4] Wisler, D. C., 1985. "Loss reduction in axial-flow compressors through low-speed model testing". *Journal of Engineering for Gas Turbines and Power,* ***107***(2), pp. 354–363. doi: 10.1115/1.3239730.

[5] Sieverding, F., Ribi, B., Casey, M., and Meyer, M., 2004. "Design of industrial axial compressor blade sections for optimal range and performance". *Journal of Turbomachinery,* ***126***(2). doi: 10.1115/1.1737782.

[6] Samad, A., and Kim, K.-Y., 2008. "Multi-objective optimization of an axial compressor blade". *Journal of Mechanical Science and Technology,* ***22***(5), pp. 999–1007. doi: 10.1007/s12206-008-0122-5.

[7] Wollmann, T., Modler, N., Dannemann, M., Langkamp, A., Nitschke, S., and Filippatos, A., 2017. "Design and testing of composite compressor blades with focus on the vibration behaviour". *Composites Part A: Applied Science and Manufacturing,* ***92***, pp. 183–189. doi: 10.1016/j.compositesa.2016.06.012.

[8] Sinha, S., and Zylka, P., 2017. "Vibration analysis of composite airfoil blade using orthotropic thin shell bending theory". *International Journal of Mechanical Sciences,* ***121***, pp. 90–105. doi: 10.1016/j.ijmecsci.2016.12.012.

[9] Mejdi, A., and Atalla, N., 2012. "Vibroacoustic analysis of laminated composite panels stiffened by complex laminated composite stiffeners". *International Journal of Mechanical Sciences,* ***58***(1), pp. 13–26. doi: 10.1016/j.ijmecsci.2012.02.003.

[10] Rocha, J., 2014. "Sound radiation and vibration of composite panels excited by turbulent flow: analytical prediction and analysis". *Shock and Vibration,* ***2014***. doi: 10.1155/2014/316481.

[11] Cherif, R., Wareing, A., and Atalla, N., 2017. "Evaluation of a hybrid TMM-SEA method for prediction of sound transmission loss through mechanically coupled aircraft double-walls". *Applied Acoustics,* ***117***(1), pp. 132–140. doi: 10.1016/j.apacoust.2016.11.002.

[12] Nordstrom, K. E., Marsh, A. H., and Sargisson, D. F., 1975. Conceptual design study of advanced acoustic-composite nacelles. Technical report NASA-CR-132703, NASA, United States. ID: 19750021020.

[13] Meo, M., Vignjevic, R., and Marengo, G., 2005. "The response of honeycomb sandwich panels under low-velocity impact loading". *International Journal of Mechanical Sciences,* ***47***(9), pp. 1301–1325. doi: 10.1016/j.ijmecsci.2005.05.006.

[14] Min, J. B., Harris, D. L., and Ting, J. M., 2012. "Advances in ceramic matrix composite blade damping characteristics for aerospace turbomachinery applications". In 52nd Structures, Structural Dynamics and Material Conference, AIAA/ASME/ASCE/AHS. doi: 10.2514/6.2011-1784.

[15] Langenbrunner, N., Weaver, M., Dunn, M., Padova, C., and Barton, J., 2015. "Dynamic response of a metal and a CMC turbine blade during a controlled rub event using a segmented shroud". *Journal of Engineering for Gas Turbines and Power,* ***137***, p. 062504. doi: 10.1115/1.4028685.

[16] Watanabe, F., Nakamura, T., and Shinohara, K.-I., 2016. "The application of ceramic matrix composite to low pressure turbine blade". In Proceedings of the ASME Turbo Expo 2016. doi: 10.1115/GT2016-56614.

[17] Corman, G., Dean, A., Brabetz, S., McManus, K., Brun, M., Meschter, P., Luthra, K., Wang, H., Orenstein, R., Schroder, M., Martin, D., De Stefano, R., and Tognarelli, L., 2001. "Rig and gas turbine engine testing of mi-CMC combustor and shroud components". In Proceedings of the ASME Turbo Expo 2001. doi: 10.1115/2001-GT-0593.

[18] Suzumura, N., Watanabe, K., Nakamura, T., Araki, T., and Natsumura, T., 2008. "Development of CMC shroud for turbine engine application". In Ceramic Engineering and Science Proceedings. doi: 10.1002/9780470294826.ch90.

[19] Storer, J. A., and Cumpsty, N. A., 1991. "Tip leakage flow in axial compressors". *Journal of Turbomachinery,* ***113***(2), pp. 252–259. doi: 10.1115/1.2929095.

[20] Sakulsaew, S., Tan, C. S., Donahoo, E., Cornelius, C., and Montgomery, M., 2013. "Compressor efficiency variation with rotor tip gap from vanishing to large clearance". *Journal of Turbomachinery,* ***135***(3), p. 031030. doi: 10.1115/1.4007547.

[21] Erler, E., Vo, H. D., and Yu, H., 2015. "Desensitization of axial compressor performance and stability to tip clearance size". *Journal of Turbomachinery,* ***138***(3). doi: 10.1115/1.4031865.

[22] Park, M., Hwang, Y.-H., Choi, Y.-S., and Kim, T.-G., 2002. "Analysis of a J69-T-25 engine turbine blade fracture". *Engineering Failure Analysis,* ***9***, pp. 593–601.

[23] Xie, Y.-J., Wang, M.-C., Zhang, G., and Chang, M., 2006. "Analysis of superalloy turbine blade tip cracking during service". *Engineering Failure Analysis,* ***13***, pp. 1429–1436.

[24] Padova, J. Barton, M. D., and Manwaring., S., 2007. "Experimental results from controlled blade tip/shroud rubs at engine speed". *Journal of Turbomachinery,* ***129***(4), pp. 713–723. doi: 10.1115/1.2720869.

[25] Millecamps, A., Brunel, J., Dufrénoy, P., Garcin, F., and Nucci, M., 2009. "Influence of thermal effects during blade-casing contact experiments". In Proceedings of the ASME 2009 IDETC & CIE conference, ASME. doi: 10.1115/DETC2009-86842 - oai: hal-01223060.

[26] Schmiechen, P., 1997. "Travelling wave speed coincidence". PhD thesis, University of London.

[27] Batailly, A., Legrand, M., Cartraud, P., and Pierre, C., 2010. "Assessment of reduced models for the detection of modal interaction through rotor stator contacts". *Journal of Sound and Vibration,* ***329***(26), pp. 5546–5562. doi: 10.1016/j.jsv.2010.07.018 - oai: hal-00524762.

[28] Sinha, S., 2004. "Dynamic characteristics of a flexible bladed-rotor with Coulomb damping due to tip-rub". *Journal of Sound and Vibration,* ***273***(4–5), pp. 875–919. doi: 10.1016/S0022-460X(03)00647-3.

[29] Lesaffre, N., Sinou, J.-J., and Thouverez, F., 2007. "Contact analysis of a flexible bladed-rotor". *European Journal of Mechanics - A/Solids,* ***26***(3), pp. 541–557. doi: 10.1016/j.euromechsol.2006.11.002.

[30] Legrand, M., Batailly, A., and Pierre, C., 2011. "Numerical investigation of abradable coating removal in aircraft engines through plastic constitutive law". *Journal of Computational and Nonlinear Dynamics,* ***7***(1), p. 011010. doi: 10.1115/1.4004951 - oai: hal-00627526.

[31] Petrov, E. P., 2012. "Multiharmonic analysis of non linear whole engine dynamics with bladed disk-casing rubbing contact". In Proceedings of the ASME Turbo Expo 2012. doi: 10.1115/GT2012-68474.

[32] Jacquet-Richardet, G., Torkhani, M., Cartraud, P., Thouverez, F., Nouri Baranger, T., Herran, M., Gibert, C., Baguet, S., Almeida, P., and Peletan, L., 2013. "Rotor to stator contacts in turbomachines. Review and application". *Mechanical Systems and Signal Processing,* ***40***(2), pp. 401–420. doi: 10.1016/j.ymssp.2013.05.010.

[33] Cuny, M., Philippon, S., Chevrier, P., and Garci, F., 2014. "Experimental measurement of dynamic forces generated during short-duration contacts: Application to blade-casing interactions in aircraft engines". *Experimental Mechanics, Society for Experimental Mechanics,* ***54***, pp. 101–114. doi: 10.1007/s11340-013-9780-z - oai: hal-01430522.

[34] Almeida, P., Gibert, C., Thouverez, F., and Ousty, J.-P., 2016. "Numerical analysis of blade disk-casing contact with friction and wear". *Journal of Engineering for Gas Turbines and Power,* ***138***(12). doi: 10.1115/1.4033065.

[35] Ma, H., Tai, X., Han, Q., Wu, Z., Wang, B., and Wen, B., 2015. "A revised model for rubbing between rotating blade and elastic casing". *Journal of Sound and Vibration,* ***337***, pp. 301–320. doi: 10.1016/j.jsv.2014.10.020.

[36] Li, B., Ma, H., Zeng, J., Guo, X., and Wen, B., 2018. "Rotating blade-casing rubbing simulation considering casing flexibility". *International Journal of Mechanical Sciences,* ***148***, pp. 118–134. doi: 10.1016/j.ijmecsci.2018.08.019.

[37] Batailly, A., and Legrand, M., 2015. "Unilateral contact induced blade/casing vibratory interactions in impellers: Analysis for flexible casings with friction and abradable coating". *Journal of Sound and Vibration,* ***348***, pp. 344–364. doi: 10.1016/j.jsv.2015.03.027 - oai: hal-01222732.

[38] Abboud, D., Elbadaoui, M., and Tableau, N., 2019. "Blade monitoring in turbomachines using strain measurements". In proceedings of the 2nd World Congress on Condition Monitoring.

[39] Craig, R. R., and Bampton, C. C., 1968. "Coupling of substructures for dynamics analyses". *AIAA Journal,* ***6***(7), pp. 1313–1319.

[40] Valdescault, A., Batailly, A., and Jones, S., 2012. *Interpolation et approximation de données à l'aide de courbes et surfaces paramétriques de type B-splines [Interpolation and approximation of data with parametric B-spline curves and surfaces].* oai: hal-00724596.